

Sparse Surface Constraints for Combining Physics-based Elasticity Simulation and Correspondence-Free Object Reconstruction

SEBASTIAN WEISS, ROBERT MAIER, RÜDIGER WESTERMANN, DANIEL CREMERS, and NILS THUEREY, Technical University of Munich, Germany

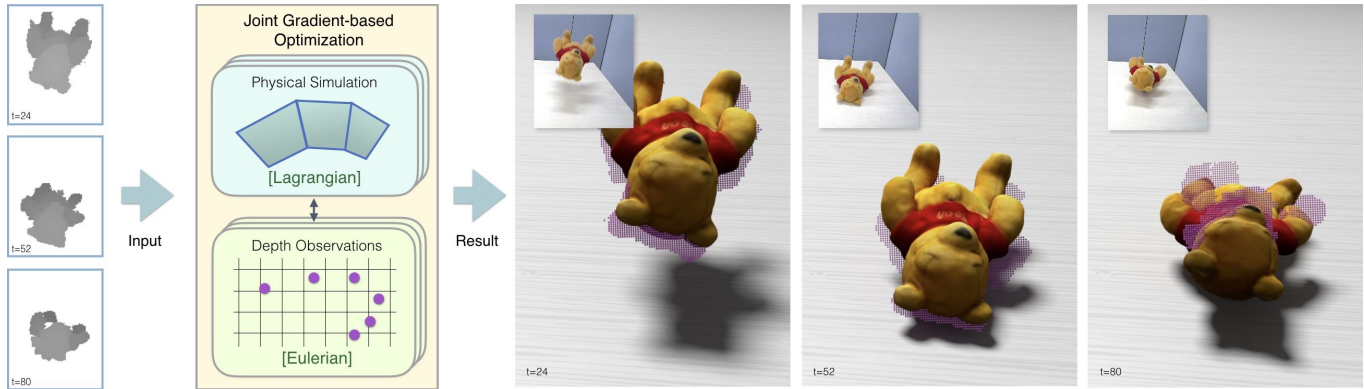


Fig. 1. Algorithm overview: From a sparse sequence of single-view depth observations, we jointly compute a physical explanation and a matching of the observations with a simulation model. In this way, we can perform an end-to-end gradient-based optimization to estimate a wide range of material parameters as well as collision geometries. The three images show a material and damping reconstruction for a plush toy. The ground truth images (not used in the optimization) are shown in the top left insets.

We address the problem to infer physical material parameters and boundary conditions from the observed motion of a homogeneous deformable object via the solution of an inverse problem. Parameters are estimated from potentially unreliable real-world data sources such as sparse observations without correspondences. We introduce a novel Lagrangian-Eulerian optimization formulation, including a cost function that penalizes differences to observations during an optimization run. This formulation matches correspondence-free, sparse observations from a single-view depth sequence with a finite element simulation of deformable bodies. In conjunction with an efficient hexahedral discretization and a stable, implicit formulation of collisions, our method can be used in demanding situations to recover a variety of material parameters, ranging from Young’s modulus and Poisson ratio to gravity and stiffness damping, and even external boundaries. In a number of tests using synthetic datasets and real-world measurements, we analyse the robustness of our approach and the convergence behavior of the numerical optimization scheme.

CCS Concepts: • **Computing methodologies** → **Physical simulation**.

Additional Key Words and Phrases: Inverse problems, soft body simulations, elasticity, surface constraints

1 INTRODUCTION

Parameterizing the deformation behavior of an object such that it can be recovered in a numerical simulation is important in many real-world applications, such as object tracking, pose estimation, and computer animation. In this work, we address the challenging inverse problem to infer the values of physical material parameters

Authors’ address: Sebastian Weiss, sebastian13.weiss@tum.de; Robert Maier, robert.maier@in.tum.de; Rüdiger Westermann, westermann@tum.de; Daniel Cremers, cremers@tum.de; Nils Thuerey, nils.thuerey@tum.de, Technical University of Munich, Arcisstraße 21, Munich, Germany.

from sparse observations, i.e., a single depth image per timestep, that can be acquired easily in real-world scenarios, e.g., with a single commodity depth camera. While previous work has likewise targeted reconstructing materials from measured deformations and visual observations, it typically relies either on carefully controlled lab settings [Bickel et al. 2009; Miguel et al. 2016; Zehnder et al. 2017], or on dense observations [de Aguiar et al. 2008; Innmann et al. 2016; Wang et al. 2015]. In contrast, we focus on real-world interactions, such as falling and colliding objects, that are recorded from a single viewpoint. Correspondingly, our goal is not a highly accurate and generic material model for fabrication or medical applications, but rather a plausible explanation that enables to analyze, understand and simulate the behaviour of objects in everyday environments.

To match sparse observations to the simulated object without an explicit feature tracking step, we propose a novel cost function that is used together with a differentiable simulation method for soft bodies. We seek to optimize for a wide range of parameters controlling the motion of an elastic body, such as Young’s modulus, Poisson ratio, mass, initial linear and angular velocity, and Rayleigh damping, as well as collision plane position and orientation. To enable the robust optimization we leverage a differentiable solver in combination with the adjoint method. The adjoint method provides analytic gradients for all matched surface points. As we will demonstrate below, this is significantly more stable than, e.g., finite differences, which have to rely on changes of the final cost function values. In addition, the adjoint method effectively allows us to optimize for multiple parameters with a negligible increase in computations, as only a single backward pass is required to simultaneously compute gradients for all parameters.

Our approach further supports the inclusion of collisions via an implicit formulation. This is important for real-world scenarios, as the collision response of materials typically contains a wide range of information for the inference of a suitable parameterization.

We take inspiration from techniques for fluid simulation, in particular, the Eulerian formulation of advective motion, and present a novel hybrid Lagrangian-Eulerian optimization algorithm. We leverage a hexahedral discretization with implicitly embedded boundaries to arrive at a simulation algorithm that is fully differentiable, and provides robust gradients for inverse problems. This makes it amenable to optimizations like the adjoint method, and a flexible tool for a variety of future algorithmic combinations, e.g., to incorporate soft body physics into deep learning methods.

The central contributions of our work target inverse elasticity problems. In this context, we propose:

- A novel formulation for sparse and correspondence-free surface constraints, e.g. measurements from RGB-D cameras.
- A hybrid Lagrangian-Eulerian approach that yields robust gradients for solving inverse elasticity problems.
- An efficient discretization scheme with implicit object boundaries and collision constraints based on a hexahedral simulation grid.

In combination, these contributions make it possible to estimate material parameters and boundary conditions in complex situations using simple hardware setups. We demonstrate this capability and analyze the plausibility of inferred results in a number of experiments using computer simulations with ground truth behavior and observed deformations of real-world objects.

2 RELATED WORK

We build upon a number of techniques in physics-based elastic body simulation: we employ linear elasticity, and a discretization based on hexahedral finite elements with a corotational formulation of strain [Dick et al. 2011; Georgii and Westermann 2008; Hauth and Strasser 2003; Müller et al. 2002]. Discretization variants and details are thoroughly discussed in previous work [Sifakis and Barbič 2015; Wu et al. 2015]. To reduce the need for very fine computational meshes, the boundary can be incorporated into the basis functions via enrichment functions [Belytschko and Black 1999]. In computer graphics, this has been used to accurately simulate cuts [Fries and Belytschko 2010; Koschier et al. 2017]. While the construction of the enrichments depends on the type of discontinuity and the interface location, the Cut Finite Element Method (*cutFEM*) makes it possible to use geometry-independent and non-boundary-fitted meshes [Hansbo et al. 2014], which is a similar concept to *Immersed Boundary Methods* for fluids [Ferstl et al. 2014; Mittal and Iaccarino 2005].

Besides the "classical" forward simulation of elastic material, a substantial amount of research has been devoted to inverse elasticity simulation. In the computer graphic community, inverse elasticity simulations are often used for artistic control. Previous works can be split into approaches that compute external forces that make the deformable body follow a prescribed animation [Barbič et al. 2009, 2012; Schulz et al. 2014], and approaches that let an elastic body deform into its rest shape via internal forces [Chen et al. 2014;

Coros et al. 2012]. Further applications of inverse methods in computer graphics include skeletal-based character animation [Kim et al. 2017], and thin shell deformations [Bergou et al. 2007]. Inverse solvers were additionally proposed for shells with friction and contact effects [Ly et al. 2018], or for reconstructing rigid body collisions [Monszpart et al. 2016].

Wang et al. [2015] instead capture motion trajectories and use virtual forces derived from these trajectories to compute an alignment between an elastic FE-mesh and the captured point cloud. The alignment procedure is split into the computation of a reference shape that best matches the observed shape, and the estimation of the deformation parameters of the captured shape. Our approach for determining material parameters from recorded depth images is inspired particularly by this work, yet instead of using a gradient-free downhill simplex method we formulate the inverse problem as a constrained minimization problem that is solved using the adjoint method [McNamara et al. 2004]. Therefore, we demonstrate the efficient calculation of the gradient of the cost function with respect to the optimization parameters at every iteration. The reconstruction from only one single depth camera as well as the integration of collisions further distinguishes our approach. We do not employ a rest pose estimation, but instead assume that it can, e.g., be obtained from an initial scan. In recent years, also first attempts have been made to replace the elasticity model itself by neural networks [Luo et al. 2018; Wang et al. 2018], an avenue that would yield interesting benefits in conjunction with algorithms for object reconstruction.

Especially for the handling of non-linear and large deformations, reduced order models have shown impressive results. Specific adaptations of linear modal bases using derivatives and modal warping have been described by Barbič and James [Barbič and James 2005] and Choi and Ko [Choi and Ko 2005], respectively. The rotation-strain space model by Pan et al. [2015] preserves the key characteristics of deformable bodies with a lower-dimensional configuration space representation. Yang et al. [2015; 2013] present a linear inertia mode technique, Xu et al. [2015] demonstrate the use of reduced models for designing material properties of three-dimensional elastic objects, and Brandt et al. [2018] enable real-time simulation of high-resolution meshes in specifically designed subspaces using projective dynamics and hyper-reduction. In some of these works, contact handling has been combined with reduced model simulation [Brandt et al. 2018; Xu et al. 2014].

Reconstructing deforming objects geometrically is a long-standing topic in research. E.g., methods were proposed to capture characters via locally rigid parts [Pekelny and Gotsman 2008], for template based capturing of freely deforming objects [Li et al. 2009], and non-rigid reconstructions based on depth videos [Innmann et al. 2016; Slavcheva et al. 2017], to name just a few. While these works share our goal to capture deforming objects, they focus on constructing a geometric representation, while our method focuses on the construction of a physical explanation for the object.

Inverse elasticity simulation has also been used in medical imaging to estimate the material properties. In the medical setting, only single physical parameters like stiffness are typically estimated. For instance, the study by Gokhale et al. [2008] use dense constraints in 2D images to estimate stiffness parameters. Kroon and Holzapfel [2008] use a similar approach including an element partitioning

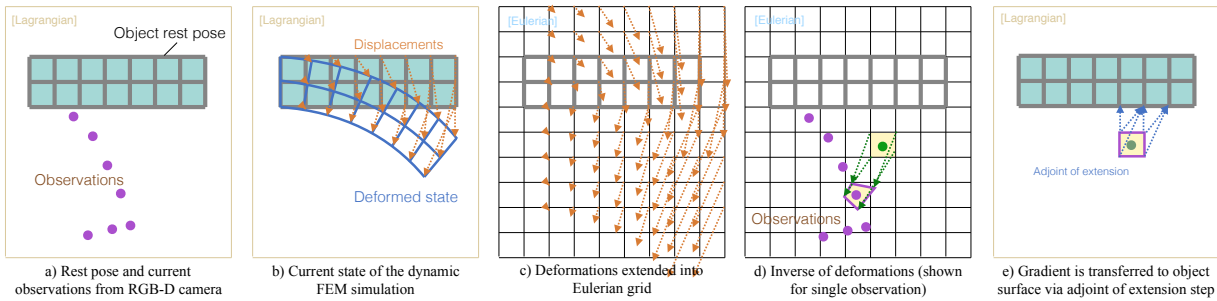


Fig. 2. Algorithm overview : Given the object in rest pose and sparse point observations, elastic displacements are first computed in an Lagrangian framework and then resampled to an Eulerian grid. For each observation, the inverse displacement is computed, and displaced observations are matched to grid cells. A cost function penalizes the distance of these observations to the object’s surface. Finally, the gradient of the cost function is transferred to the object surface via the adjoint of the extension step.

strategy to estimate elastic properties. Posterior distributions over linear elastic material parameters are estimated via Monte-Carlo Markov-Chain by Risholm *et al.* [2011], while inhomogeneous elasticity parameters of shell-like surface structures are targeted by Zhao *et al.* [2017]. Similar approaches have been used in computer graphics to capture complex materials, e.g., to design deformable objects for fabrication Bickel *et al.* [2010; 2009], and to obtain accurate parameterizations of cloth behavior Wang *et al.* [Wang et al. 2011]. More recently, researchers have also investigated building libraries of material behavior [Chen et al. 2015] and measuring complex and non-uniform materials [Miguel et al. 2016; Zehnder et al. 2017]. Although the works above share our overall goals and achieve impressive material estimates, they inherently rely on full correspondences between observations and the geometric models, and thus are difficult to apply outside of lab environments.

3 OVERVIEW AND PHYSICAL MODEL

We assume that a scanned representation of the observed object in rest pose exists. At the core of our method, we iteratively optimize the physical parameters that govern the object’s deformation behavior. In a forward step, a Lagrangian elasticity simulation is performed with the current parameter estimates. We use a finite element discretization of the displacement field with tri-linear shape functions, and employ a rotational invariant formulation of the strain tensor using the corotated strain formulation. The computed deformations are then matched and compared to a set of observations, e.g. given by depth images from a commodity RGB-D sensor. This step utilizes a Cartesian grid as Eulerian representation, which is facilitated by the hexahedral Lagrangian discretization used in the forward simulation. The matching step, constrained by the physical deformation properties, provides a similarity measure and enables the calculation of gradients of the cost function that is to be minimized. These gradients are back-traced through the simulation using the adjoint method, in order to obtain updates for the physical parameters via a gradient-based optimizer. This process is illustrated in Fig. 2. The parameters that can be reconstructed are gravity, Young’s modulus, Poisson ratio, mass and stiffness damping and the collision plane position. For example, optimizing for the collision plane allows us to reconstruct collisions even if the actual point of impact is obstructed

from the camera. Due to the inherent non-linearity, we evaluate a batch of optimization runs using perturbed initial values, and choose the best match as final result.

In the following, we briefly summarize the used elasticity model. Details of our particular discretization scheme are provided in Sec. 6. The reference configuration of the observed, scanned object is given as a signed distance function (SDF) $\phi_0 : \mathbb{R}^3 \rightarrow \mathbb{R}$ with the object occupying the space where ϕ is negative: $\Omega_r := \{\mathbf{x} \in \mathbb{R}^3 : \phi_0(\mathbf{x}) < 0\}$. For a displacement of each point of the object at time $t \geq 0$ ($t \in \mathbb{R}_0^+$) given by $u : \Omega^r \times t \rightarrow \mathbb{R}^3$, the linear *Green strain tensor* $E(u) := \frac{1}{2}(\nabla u + (\nabla u)^T)$ is used to compute the second order *Piola-Kirchhoff stress tensor* as $P(u) := 2\mu E(u) + \lambda \text{tr}(E(u))\mathbf{1}$, with the *Lamé coefficients* μ and λ derived from the Young’s modulus k and the Poisson ratio ρ . The dynamic behavior of a deformable object is then governed by the system of partial differential equations

$$m\ddot{u} - \text{div} P(u) = f_B \quad \text{in } \Omega^r \times \mathbb{R}_0^+ \quad (1a)$$

$$u = u_D \quad \text{on } \Gamma_D^r \times \mathbb{R}_0^+ \quad (1b)$$

$$P(u) \cdot \mathbf{n} = f_S \quad \text{in } \Gamma_N^r \times \mathbb{R}_0^+ \quad (1c)$$

The body forces are denoted by f_B and include e.g. the gravity. The boundary conditions on the boundary Γ_D^r consist of Dirichlet boundary conditions, which prescribe the displacement u_D on Γ_D^r , and Neumann boundary conditions, which prescribe external surface forces f_S on Γ_N^r . \mathbf{n} is the unit outer normal on Γ_N^r , and m the body’s mass. For the dynamic case, this leads to an initial value problem, using the initial shape ϕ_0 and material parameters. In our work, problem (1) is discretized in space using a hexahedral simulation grid with implicitly embedded boundaries, and in time by applying a Newmark time integration scheme.

4 SPARSE SURFACE CONSTRAINTS

The goal of our work is to estimate unknown material parameters from observed object deformations with an optimization algorithm. One fundamental problem is to find a cost function J that can reliably and efficiently penalize differences to observations. We first review existing cost functions in order to motivate our proposed cost function.

4.1 Existing Cost Functions

A natural choice for a cost function is one that considers squared differences of per-vertex displacements and derivatives over time t , as illustrated in Fig. 3b and proposed in previous works [Coros et al. 2012; Pan and Manocha 2018]:

$$J_{\text{DISP}}(u) := \sum_{t=1}^T \frac{1}{2} w_t \left\| u^{(t)} - u_{\text{obs}}^{(t)} \right\|_{\Omega^r}^2 + \frac{1}{2} v_t \left\| \dot{u}^{(t)} - \dot{u}_{\text{obs}}^{(t)} \right\|_{\Omega^r}^2. \quad (2)$$

Here, u_{obs} denotes observed positions, e.g., from a tracking procedure. The weighting terms w_t, v_t are optional to, e.g., model the reliability of measurements. This cost function requires ground truth vertex displacements, which are often not available. Feature tracking methods [Schulman et al. 2013; Wang et al. 2015] can circumvent this problem by explicitly matching observations to vertices in the simulation mesh. However, the matching step does not provide derivatives, and as such cannot be used in conjunction with gradient-based optimization schemes. In addition, explicit matching approaches typically only couple to a simulation via external force estimates, and are thus decoupled from the actual parameter estimation step. Errors in the computed vertex displacements will invariably propagate into the inferred physical simulation.

Another cost function variant that is especially popular for fluid control uses squared differences of the SDF values ϕ per domain point [McNamara et al. 2004]. The function can be formulated as

$$J_{\text{SDF}}(\phi^{(t)}) := \sum_{t=1}^T \frac{1}{2} \left\| w_t \left(\phi^{(t)} - \phi_{\text{obs}}^{(t)} \right) \right\|_{\Omega}^2, \quad (3)$$

with ϕ_{obs} denoting the observation, i.e. a target SDF in this case. The SDF-based cost function, however, requires a full SDF representation $\phi^{(t)}$, and while guesses about the complete 3D shape of the observation could be made, erroneous estimates can easily mislead the optimization procedure. Furthermore, the current SDF $\phi^{(t)}$ needs to be calculated by means of an advection step from ϕ_0 and $u^{(t)}$, e.g., with a semi-Lagrangian method. While this is possible in general, it requires highly non-linear gradient evaluations for inverting the displacement field, which often leads to diverging optimizations in practice. This is demonstrated in Fig. 3c, where even for the simple 2D setup the gradients increasingly deteriorate for lower values of the Young’s modulus.

4.2 Proposed Cost Function for Sparse Surface Constraints

We instead propose a SDF-based formulation that is able to incorporate sparse constraints without requiring any explicit feature matching. We assume that in time step t , $N^{(t)}$ points—with world space positions $\mathbf{x}_{t,i} \in \mathbb{R}^3$ —are observed via depth images. Here, we denote single vectors in bold face, e.g., \mathbf{x} , while vector fields are denoted with non-bold letters as before. Since observed points are located at the object boundary where $\phi = 0$, our new *sparse surface constraint* (SSC) cost function aims to minimize the SDF values at these locations via

$$J_{\text{SSC}}(\phi) := \sum_{t=1}^T \sum_{i=0}^{N^{(t)}} w_{t,i} \frac{1}{2} \left(\phi^{(t)}(\mathbf{x}_{t,i}) \right)^2. \quad (4)$$

To avoid advecting the full SDF, we introduce a new method that intrinsically encapsulates our underlying sparseness assumption by solving for a point-wise inversion of the body motion. This method builds upon the assumption that the simulated displacements $u^{(t)}$ do not destroy the signed distance property of ϕ . Then we can approximate $\phi^{(t)}$ —the deformed SDF— by evaluating the initial SDF at the images of displaced locations, i.e., by going along the inverse displacement field, without the need to reinitialize the SDF:

$$\phi^{(t)}(\mathbf{x}) \approx \phi^{(0)} \left(\mathbf{x} + u^{(t)}(\mathbf{x})^{-1} \right), \quad (5)$$

where $u(\mathbf{x})^{-1}$ indicates the inverse function, i.e. $\mathbf{y} = u(\mathbf{x})^{-1} \rightarrow \mathbf{x} = u(\mathbf{y})$. However, this requires the inverse displacement field, which cannot simply be computed by back-tracing as in divergence-free fluid flows. Since every point \mathbf{x} of the deformed object can be associated with a matching point \mathbf{x}' of the undeformed object, the problem can be reformulated in the following way: Since we know the point \mathbf{x} with $\mathbf{x} = \mathbf{x}' + u^{(t)}(\mathbf{x}')$ (and hence $\mathbf{x}' = \mathbf{x} + u^{(t)}(\mathbf{x})^{-1}$), we can compute the (yet unknown) index (i, j, k) of the hexahedral simulation cell containing \mathbf{x}' . With $\mathcal{N} = \{i + [0, 1], j + [0, 1], k + [0, 1]\}$ denoting the eight corners of the cell (i, j, k) , and $\mathbf{x}'_{l \in \mathcal{N}}$ their reference locations, let $\mathbf{x}_{l \in \mathcal{N}}$ be the displaced locations of these corners, i.e., $\mathbf{x}_l = \mathbf{x}'_l + \mathbf{u}_l^{(t)}$. Then, the location of point \mathbf{x}' can be computed by trilinear interpolation of the eight reference corner locations, with the cell-wise interpolation weights α, β, γ .

By further assuming that the interpolation weights don’t change during the advection, i.e., \mathbf{x}' is interpolated from \mathbf{x}'_l with the same weights as \mathbf{x} is interpolated from \mathbf{x}_l (see Fig. 4), the same weights for interpolating positions can be used to interpolate the SDF values. This allows us to formulate Alg. 1 for computing $\phi^{(t)}(\mathbf{x})$:

Algorithm 1 Compute $\phi^{(t)}(\mathbf{x})$ based on $\phi^{(0)}$ and $u^{(t)}$

Input: The observed point \mathbf{x}
1: **for each** cell i, j, k **do**
2: Compute α, β, γ with Newton solve of
3: $\mathbf{x} = \text{interpolate}(\mathbf{x}_{l \in \mathcal{N}}, \alpha, \beta, \gamma)$
4: **if** $(\alpha, \beta, \gamma) \in [0, 1]^3$ **then**
5: **return** $\phi^{(t)}(\mathbf{x}) = \text{interpolate}(\phi_{l \in \mathcal{N}}^{(0)}, \alpha, \beta, \gamma)$
6: **end if**
7: **end for**

The key step here is solving for the unknown trilinear interpolation weights. This requires finding a solution within the cell space $[0, 1]^3$ of a non-linear system of equation in three variables. For this, we employ a Newton iteration that typically converges within a few iterations. Recall that the standard trilinear interpolation is given as

$$\begin{aligned} f(\alpha, \beta, \gamma) &= (1 - \alpha)(1 - \beta)(1 - \gamma)\mathbf{x}_1 + \alpha(1 - \beta)(1 - \gamma)\mathbf{x}_2 \\ &\quad + \cdots + \alpha\beta\gamma\mathbf{x}_8 \\ &= \mathbf{z}_1 + \alpha\mathbf{z}_2 + \beta\mathbf{z}_3 + \gamma\mathbf{z}_4 + \alpha\beta\mathbf{z}_5 + \alpha\gamma\mathbf{z}_6 + \beta\gamma\mathbf{z}_7 \\ &\quad + \alpha\beta\gamma\mathbf{z}_8. \end{aligned} \quad (6)$$

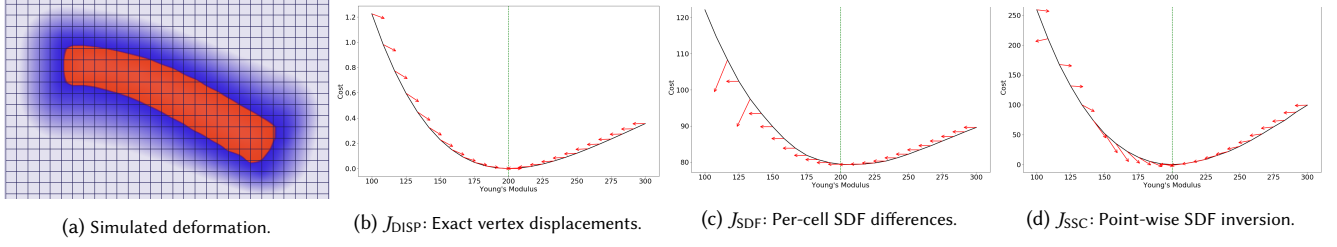


Fig. 3. Comparison of cost functions for the elastic simulation in (a). (b) Known vertex correspondences enable accurate gradient estimation. (c) Per-cell SDF differences give mostly wrong gradient estimates due to the highly non-linear advection step: For a Young’s modulus less than 200 the gradients all point into the wrong direction. (d) By using the proposed cost function J_{SSC} , almost everywhere can the gradients be recovered accurately.

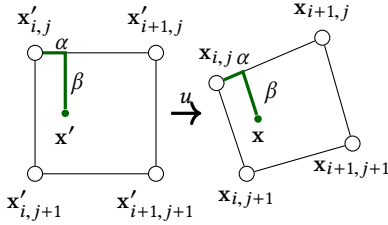


Fig. 4. Interpolation for reference and deformed configurations.

Then, a Newton iteration is computed as $\alpha\beta\gamma^{t+1} = \alpha\beta\gamma - J^{-1}f(\alpha\beta\gamma^t)$, with

$$J = \begin{pmatrix} z_2 + \beta z_5 + \gamma z_6 + \beta\gamma z_8 & \cdots \end{pmatrix}. \quad (7)$$

being the Jacobian.

In case of a self-intersection, it can happen that a single observed point \mathbf{x} is located in two different cells. Upon detecting this case we match the cell with the lowest interpolated SDF-value $\phi^{(t)}(\mathbf{x})$.

4.3 Extension of Displacements

To ensure that J_{SSC} can be evaluated for all cells that possibly contain an observed point, the displacements, which are provided by the FE solver only at locations covered by the object, need to be extended into the ambient space around the object. For that purpose, we extend the displacements around the rest pose on the Eulerian grid via a solving a Poisson problem for a diffusion process. As is commonly done, e.g., for level-set methods [Osher and Fedkiw 2006], the extension is only performed in a narrow band around the surface. The width of the narrow band ϕ_{\max} naturally defines an upper bound per point for our cost function. The width specifies the maximum allowed distance of a matched point to the surface. Thus, points that are further away from the surface can be ignored and induce a constant cost of $\frac{1}{2}\phi_{\max}^2$. All cells that receive displacements are implicitly matched with observations via the SSC. Once observations and displacements are brought together, the adjoint method ensures that the information travels back to the relevant nodes on the FE mesh. This process is visualized in Fig. 2c) to e). Note that this two-step process – extension first, then matching via deformation – differs from standard procedure in Eulerian solvers [Bridson, R.

2015] and in previous work [Wang et al. 2015]. There, the object itself is typically deformed, and correspondences established with the deformed state. We found that the latter variant is not suitable for gradient-based optimizations, the primary reason being the inherently divergent displacement field of the deformable object, which precludes the use of commonly used methods for advection. This variant corresponds to the aforementioned J_{SDF} formulation, and an example of the sub-par gradients it yields can be seen in Fig. 3c). Hence, our reconstructions will focus on J_{SSC} in the following.

While for convex objects ϕ_{\max} can be chosen arbitrarily, for concave objects like the dragon in Figure 9 the narrow band can self-penetrate leading to points that cannot be matched uniquely to the surface via the adjoint method. Therefore, in all our experiments we heuristically limit ϕ_{\max} to approximately half the size of the smallest cavity. A more detailed quantitative evaluation of how this parameter influences the accuracy of the solutions can be found in Appendix C.3. If a small value for ϕ_{\max} was chosen, it can happen that no points can be matched, especially for later time steps when the current simulation is far away from the observations. This does not pose a problem for our optimization as long as early time steps tie the simulation to the observations. As the optimizer converges towards a tighter match between observations and cells, more and more points from later timesteps are included in the cost function and improve the results.

To summarize, with one pass over the computational grid, we can compute the inverse mappings (as interpolation weights) for all observed points \mathbf{x} , so that J_{SSC} can be evaluated. All steps in the evaluation of J_{SSC} , as well as the extension step, can be efficiently differentiated and incorporated into an inverse elasticity solver for optimizing the material parameters. Fig. 3d demonstrates the capability of J_{SSC} to accurately estimate gradients.

5 INVERSE ELASTICITY SOLVER

By using a forward solver for Eq. (1) in combination with our proposed cost function J_{SSC} , we propose an optimization framework for the unknown material parameters using the adjoint method [McNamara et al. 2004]. Let $\mathbf{u} \in \mathbb{R}^U$ be the $U \in \mathbb{N}$ states of the system, i.e., the output variables such as the computed displacements $u^{(t)}$ and velocities $\dot{u}^{(t)}$ for each timestep. Let $\mathbf{p} \in \mathbb{R}^P$ be the P control parameters of the system, i.e., the estimated material parameters

that are used as input variables in the forward pass. The general optimization problem is then defined as

$$\text{minimize } J(\mathbf{u}, \mathbf{p}), \quad J: \mathbb{R}^U \times \mathbb{R}^P \rightarrow \mathbb{R} \quad (8a)$$

$$\text{subject to } \mathbf{E}(\mathbf{u}, \mathbf{p}) = \mathbf{0}, \quad \mathbf{E}: \mathbb{R}^U \times \mathbb{R}^P \rightarrow \mathbb{R}^U \quad (8b)$$

with a problem-specific function $\mathbf{E}(\mathbf{u}, \mathbf{p})$ that relates the control parameters to the state variables and a cost function $J(\mathbf{u}, \mathbf{p})$. The gradient $\frac{dJ}{d\mathbf{p}}$, which is needed in the optimization, is computed by first solving

$$\frac{\partial \mathbf{E}}{\partial \mathbf{u}} \mathbf{y} = \frac{\partial J}{\partial \mathbf{u}}, \quad (9)$$

for \mathbf{y} , and then computing

$$\frac{dJ}{d\mathbf{p}} = -\mathbf{y}^T \frac{\partial \mathbf{E}}{\partial \mathbf{p}} + \frac{\partial J}{\partial \mathbf{p}}. \quad (10)$$

The advantage of the adjoint method is that just a single linear system (Eq. (9)) has to be solved initially. Afterwards, arbitrary control parameters can be added to the final vector-matrix multiplication (Eq. (10)). Therefore, the computational cost of a single gradient evaluation is mostly independent of the number of control parameters.

For a problem that can be formulated as a sequence of function calls

$$\mathbf{x}_1 \leftarrow f_1(\mathbf{x}_0) \quad (11a)$$

$$\mathbf{x}_2 \leftarrow f_2(\mathbf{x}_1) \quad (11b)$$

...

the general problem matrix \mathbf{E} becomes triangular and the adjoint step, i.e., Eq. (9) and (10), simplifies to [McNamara et al. 2004]

...

$$\hat{\mathbf{x}}_1 \leftarrow \hat{\mathbf{x}}_2 + \left(\frac{\partial f_2(\mathbf{x}_1)}{\partial \mathbf{x}_1} \right)^T \hat{\mathbf{x}}_2 \quad (12a)$$

$$\hat{\mathbf{x}}_0 \leftarrow \hat{\mathbf{x}}_1 + \left(\frac{\partial f_1(\mathbf{x}_0)}{\partial \mathbf{x}_0} \right)^T \hat{\mathbf{x}}_1. \quad (12b)$$

Here, $\hat{\mathbf{x}}$ denotes the adjoint of a variable, which stores the accumulated gradient $\hat{\mathbf{x}}$. Taking the adjoint of an operation f means applying the transposed derivative, as shown in Eq. (12). An overview of the different steps that are considered in the adjoint method is depicted in Fig. 5.

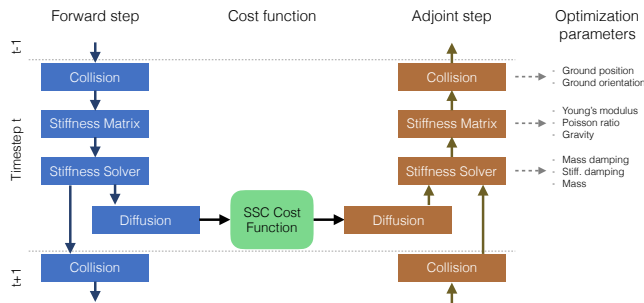


Fig. 5. Outline of the forward and adjoint steps.

In each time step, the system matrix \mathbf{E} in Eq. (8b) captures collision handling (subsection 6.2), stiffness matrix assembly with corotation (App. A.1), stiffness solve (subsection 6.1) and displacement extension (subsection 5.1). In the adjoint pass, the order of operations is reversed. Starting from the last frame, the adjoint variables of the displacements and velocities are computed with the derivatives of the operations $\frac{\partial \mathbf{E}}{\partial \mathbf{u}}$. This gives the adjoint state \mathbf{y} in Eq. (9). Instead of computing the gradients of the control parameters afterwards as in the general adjoint method Eq. (10), we found it to be more efficient to assemble the gradients directly within the respective adjoint operations as indicated in Fig. 5 and Eq. (12).

5.1 Sparse Surface Constraint: Gradient Evaluation

Our cost function formulation allows for an efficient gradient calculation within the adjoint framework. From the forward problem in Alg. 1, the index of the cell that contains an observed point \mathbf{x} is known. Then, computing the adjoint of the trilinear interpolation with respect to the interpolation weights is straight forward, yet computing the adjoint of the inverse of the interpolation, i.e. solving for the weights, is more challenging. In principle, we could mechanically compute the adjoint of the Newton iteration, but a much simpler solution can be derived by taking the derivative of the tri-linear interpolation as a whole. Therefore, let us express the cell-wise interpolation as \mathbf{E} from the adjoint method:

$$\mathbf{E}(\mathbf{u} = \{\alpha, \beta, \gamma\}, \mathbf{p} = \{\mathbf{z}_1, \dots, \mathbf{z}_8\}) := \mathbf{z}_1 + \alpha \mathbf{z}_2 + \beta \mathbf{z}_3 + \gamma \mathbf{z}_4 + \alpha \beta \mathbf{z}_5 + \alpha \gamma \mathbf{z}_6 + \beta \gamma \mathbf{z}_7 + \alpha \beta \gamma \mathbf{z}_8 - \mathbf{x} = \mathbf{0},$$

Then, the matrix

$$\mathbf{A} = \frac{\partial \mathbf{E}}{\partial \mathbf{u}} = \begin{pmatrix} | & | & | & | & | & | & | & | \\ \mathbf{z}_2 + \beta \mathbf{z}_5 + \gamma \mathbf{z}_6 + \beta \gamma \mathbf{z}_8 & \dots & \dots & \dots & \dots & \dots & \dots & \dots \\ | & | & | & | & | & | & | & | \end{pmatrix} \in \mathbb{R}^{3 \times 3}.$$

is exactly the same matrix that is used in the Newton iteration in Alg. 1. Next, the derivative of the trilinear interpolation with respect to the control points $\mathbf{p} = (\mathbf{z}_1, \dots, \mathbf{z}_8)$ is computed as

$$\mathbf{F} = \frac{\partial \mathbf{E}}{\partial \mathbf{p}} = - \begin{pmatrix} | & | & | & | & | & | & | & | \\ 1 & \alpha & \beta & \gamma & \alpha \beta & \alpha \gamma & \beta \gamma & \alpha \beta \gamma \\ | & | & | & | & | & | & | & | \end{pmatrix} \in \mathbb{R}^{3 \times 8}.$$

With this matrix, the adjoint variables of \mathbf{z}_1 to \mathbf{z}_8 are computed as $(\hat{\mathbf{z}}_1, \dots, \hat{\mathbf{z}}_8) = (\alpha', \beta', \gamma') \mathbf{F}$. Finally, the adjoint values $\hat{\mathbf{z}}_1, \dots, \hat{\mathbf{z}}_8$ are added to the adjoint values of the per-vertex displacements $\hat{\mathbf{u}}_{i,j,k}, \dots, \hat{\mathbf{u}}_{i+1,j+1,k+1}$, by taking the adjoint of the mapping from $\mathbf{x}_1, \dots, \mathbf{x}_8$ to $\mathbf{z}_1, \dots, \mathbf{z}_8$ (Eq. (6)).

Our cost function yields gradients on the whole computational grid. The gradients are transferred back to the active nodes with the adjoint of the Eulerian extensions of the displacements.

If the current state of the simulation shows large differences to the observations, some points are matched with cells that lie outside the object. The adjoint of the extension then "pulls back" the gradients from these points onto the object's surface, and connects them to the Lagrangian simulation. We refer to the Appendix for a discussion of how to compute the gradients of the damping parameters. The lengthy description of how the remaining gradients are computed is omitted here. It will be provided together with the source code of our implementation.

6 FEM DISCRETIZATION

The deformable body is discretized by means of hexahedral elements with trilinear shape functions, which are aligned on a regular Cartesian grid. We further embed the object boundary into the simulation grid, and consider cells that are partly filled with material (see Appendix A.1). Physical properties like Young’s modulus and Poisson’s ratio are specified globally for simplicity, but could be assigned on a per-element basis. The hexahedral discretization yields simplified expressions of the stiffness terms, i.e., since all elements have the same shape, the same stiffness matrix can be used for all of them (up to scaling according to the respective element’s elastic modulus). Thus, we require only a single element stiffness matrix and can significantly accelerate the setup phase for the simulation. Since the discretization always refers to the undeformed model state, no further calculations are required even if the object geometry deforms and hexahedra become of different shapes. The whole simulation is executed on the GPU using *cuMat* [Weiss, S. 2018] as linear algebra library. Furthermore, and as described in Sec. 4, an Eulerian discretization of the space around the object can be obtained from a hexahedral discretization in a straight forward way, and sparse point sets can be included as observations without requiring explicit feature matching.

6.1 Time integration

Once the stiffness matrix K , the mass matrix M and the force vector f are assembled from the per-element matrices, we introduce Raleigh damping via the matrix D , and solve the resulting linear system

$$M\ddot{u} + D\dot{u} + Ku = f \quad (13)$$

with a Newmark scheme that takes the following form [Greenough 2001]:

$$\begin{aligned} & \left(\frac{1}{\theta\Delta t} M + D + \theta\Delta t K \right) u^{(t)} \\ &= \left(\frac{1}{\theta\Delta t} M + D + (1-\theta)\Delta t K \right) u^{(t-1)} + \frac{1}{\theta} M\dot{u}^{(t-1)} + \Delta t f \end{aligned} \quad (14)$$

with $\frac{1}{2} \leq \theta < 1$ and

$$\dot{u}^{(n)} = \frac{1}{\theta\Delta t} (u^{(t)} - u^{(t-1)}) - \frac{1-\theta}{\theta} \dot{u}^{(t-1)}. \quad (15)$$

If f is time-dependent, it is given as

$$f = \theta f^{(t)} + (1-\theta)f^{(t-1)}. \quad (16)$$

Here, time-splitting of the forces in Eq. (16) is required to make the collisions numerically stable.

The hyper-parameter θ in the Newmark time integration scheme was set to 0.6 in all of our experiments. As confirmed by a number of tests, values of θ between 0.5 and 0.75 do not result in any noticeable differences. Only for large timesteps and low Rayleigh damping does a large value of $\theta = 0.99$ introduce undesirable damping. For a comparison of different values of θ we refer to the supplemental video.

6.2 Collisions

In order to include collisions in our inverse solver framework, we employ the penalty method [Bridson et al. 2002; Coros et al. 2012]. Wherever the object penetrates another object, e.g. a ground plane, a virtual spring is attached to it that generates a repulsive force that is added as a Neumann boundary in the next timestep.

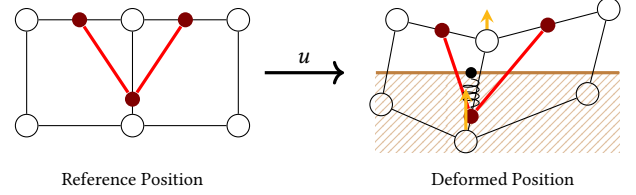


Fig. 6. Collision handling in the hexahedral FEM simulation.

Let $x = \text{dist}(\mathbf{x})$ be the penetration depth of point \mathbf{x} . Then, the force of a spring is described by Hooke’s Law: $\mathbf{f} = -kx\mathbf{n}$ with the stiffness factor k and outer normal vector \mathbf{n} . In our case, the spring must not exert an attractive force towards the surface when the objects are not penetrating. Therefore, the force has to be clamped:

$$\mathbf{f}_c = -k \min(0, x)\mathbf{n}. \quad (17)$$

To obtain a stable simulation, we propose the following two improvements over previous approaches using repulsive forces as collision response. First, the hard minimum in Eq. (17) is replaced by a soft minimum [Cook 2010; Mächler 2012]

$$\begin{aligned} \mathbf{f}_c &= -k \text{softmin}(0, x)\mathbf{n} \\ &\text{with } \text{softmin}_\alpha(a, b) := -\ln(e^{-a\alpha} + e^{-b\alpha})/\alpha. \end{aligned} \quad (18)$$

Note that this step makes the minimum differentiable, which is necessary to consider the collision response in the adjoint method.

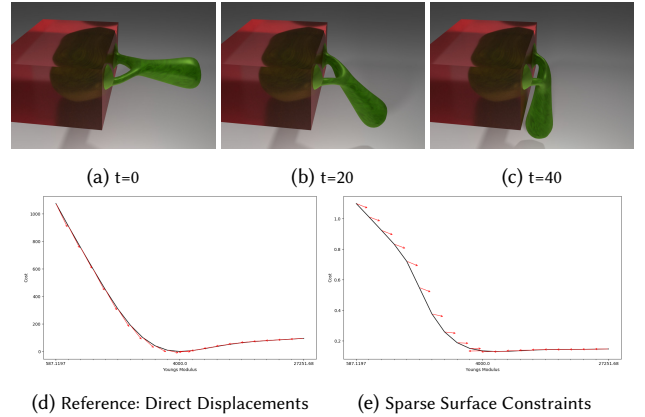


Fig. 7. Three selected frames (a-c) of a bending tree simulation. Cost functions and gradients for optimizing for Young’s modulus (ground truth of 4000) using Direct Displacements as reference (d) and cost function J_{SSC} (e). Sparse Surface Constraints were evaluated every 10th timestep, using one single camera with Gaussian noise variance of three voxels. Gradients robustly point into the direction of the ground truth.

Second, the collision forces have to be included implicitly in the Newmark integrator, i.e., Eq. (16). However, since the collision force at the next timestep $\mathbf{f}_c^{(n)}$ is not known, it is approximated using the time derivative of Eq. (18) as

$$\mathbf{f}_c^{(n)} \approx \mathbf{f}_c^{(n-1)} + \Delta t \frac{\partial}{\partial t} \mathbf{f}_c^{(n-1)}. \quad (19)$$

The accompanying video shows the influence of this collision formulation for a dynamic simulation.

7 RESULTS AND EVALUATION

In the following, we analyze the accuracy, robustness behavior and performance of our approach. All of our experiments were performed on a desktop system equipped with an Intel Xeon W-2123 CPU, 64 GB RAM and a Nvidia RTX 2070 GPU. We analyze both synthetic datasets, to be able to compare to ground truth material parameters, as well as live captures of a fallen teddy bear and a pillow. If not otherwise mentioned, synthetic datasets are forward simulated using the described finite-element scheme, and depth images are rendered and provided as sparse constraints. For the live captures we demonstrate how well a forward simulation with the estimated parameters recovers the recorded body dynamics. Setup parameters for all experiments are given in Table 2. We show forward simulations by rendering a triangle mesh that is deformed with the simulated displacements.

7.1 Gradient estimation

First, we analyze the capability of the new cost function J_{SSC} to deal with sparse observations and to provide reliable gradients. Our key observation is that the proposed formulation is very robust against sparsity of observations and noise, and that only the absolute cost values become increasingly unstable with increasing sparsity and noise level. As an example we use a bending tree model (see Fig. 7a-c), simulated over 70 timesteps, and we synthesize observations using a camera resolution of 50×50 . The object is fixed via Dirichlet boundaries, shown as red box, while the green region freely moves under the influence of gravity. In the reference forward simulation, the Young’s modulus was set to 4000. Fig. 7 shows the cost function and resulting gradients (red arrows) for varying Young’s moduli. The gradients reliably pull back the Young’s modulus to the target value of 4000. J_{SSC} and gradient estimation performed equally well for other test cases.

Fig. 7d shows the behavior when J_{disp} from Eq. (2) is evaluated directly on corresponding vertices. Even though these correspondences cannot be determined in general, we use the resulting convex cost function with smooth gradients as reference. We then simulate a real-world setting: Only one camera is used, the camera provides observations only every 10th timestep as the framerate is often limited, and the observations are affected by noise. The proposed Sparse Surface cost function can still accurately determine the gradients as shown in Figure 7e.

Next, we perform tests with the torus data set (see Figure 8) to analyze the stability of the optimizer over an increasing number of timesteps and noise magnitudes. A detailed analysis for this as well as the following experiments can be found in Appendix C.1 and C.2. Our experiments demonstrate that, although numerical

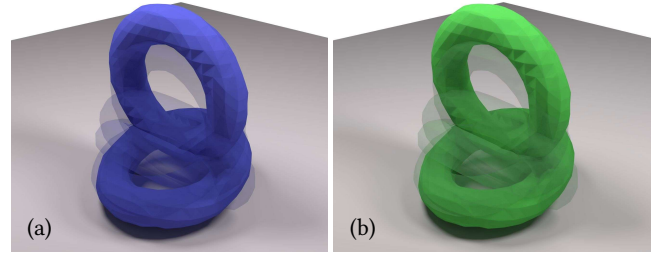


Fig. 8. We reconstruct the material properties of a synthetic elastic torus bouncing off the ground floor with our method. Simulation using our reconstruction in green (b) very closely matches the ground truth (a). The two solid tori depict the simulation state at time $t = 0$ and $t = 40$, the transparent frames are in-between frames.

errors accumulate over multiple timesteps, the gradients still reliably point towards the minimum so that the ground truth can be reconstructed. Furthermore, we show that increasing noise in the observation does not deteriorate the stability of our method.

Finally, we highlight that the adjoint method is crucial for our method by comparing it to a finite difference scheme. Our experiments clearly demonstrate a significantly improved robustness of the adjoint optimization compared to the finite difference method. Optimization runs using the finite difference scheme typically converge to local minima and fail to reconstruct the ground truth value (details are given in Figure 24 in the Appendix). Intuitively, the adjoint method evaluates the gradient of each observed point locally and back-traces the gradient via our differentiable solver, independent of the number of matched points. In this way, robust optimizations are achieved. Besides lower robustness, the following two disadvantages of the finite difference method for computing gradients are worth mentioning: Firstly, it requires one separate forward pass for every parameter instead of one single backward pass for all parameters as with the adjoint method. Secondly, it requires an additional hyper-parameter to specify the step size for finite difference computations.

7.2 Different Optimizers

In combination with our proposed cost function J_{SSC} the following optimizers were tested:

- A simple gradient descent (GD) method with adaptive stepsize control [Fletcher 2005].
- The R-Prop algorithm [Riedmiller and Braun 1993] that uses the direction of the gradients ignoring their magnitudes.
- The standard L-BFGS algorithm [Byrd et al. 1995] as implemented in *Eigen* [Qiuv, Y. 2016].

In a number of experiments given in Appendix C.7 we show superior stability of the R-Prop algorithm. For optimizations with a single parameter, both GD and R-Prop find the global optimum, whereas L-BFGS tends to overshoot the optimum and gets stuck in a local minimum. The experiments were performed on synthetic data sets for which ground truth parameters exist (Figure 9 and Figure 11). For multi-parameter optimization, R-Prop outperforms all other methods and finds the local minimum with the lowest cost.

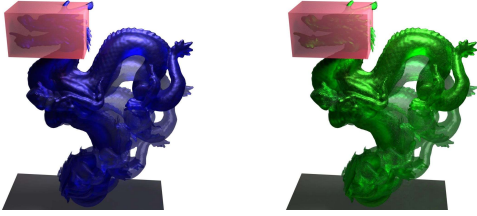


Fig. 9. Our proposed cost function J_{SSC} is especially suitable for complex geometries. These images show a ground truth simulation (a) and our reconstruction (b), which yields very small reconstruction errors, leading to a visually indistinguishable result.

7.3 Synthetic tests

In order to demonstrate the accuracy and robustness of our method, we evaluated the performance of the optimization framework on two synthetic examples with known ground truth values: a torus (Figure 8) and a bouncing ball (Figure 11). Our first set of tests (see Appendix C.4) indicate that our optimization works robustly even with very few cameras and very low resolutions, i.e. sparse observations. 20×20 depth values were sufficient to reconstruct the ground truth state in 18 out of 20 runs, which increases to 20 out of 20 for a resolution of 100×100 . Convergence plots for varying numbers of cameras and resolutions of depth images are given in Fig. 10. The plots show that our method yields the ground truth Young’s modulus in the vast majority of cases. The relative errors (averaged over all converged runs) is 2.39% and 5.08% for 4 and 1 camera, respectively, and 2.71% and 3.05% for 100×100 and 20×20 depth images, respectively.

In a second set of tests (see Appendix C.5), we demonstrate that the optimization is very robust against changes in the boundary conditions. We let a ball with constant material properties bounce off a ground plane. The ball’s initial velocity and the height and orientation of the ground plane are randomly sampled. For all settings, the optimization converges in 18 to 20 cases of 20 runs in total, several examples of which are shown in Fig. 11. In addition, our approach can handle complex geometries. We evaluate a synthetic data set for a deformable Stanford dragon, as shown in Fig. 9.

A final test (see Appendix C.6) sheds light on how stable multiple parameters can be jointly optimized by the optimization process. Again, we let a ball bounce off a ground plane, but this time optimize jointly for gravity, the Young’s modulus and the stiffness damping. While gravity is estimated exactly, the Young’s modulus and stiffness damping show a wide range of values. At the same time, however, all runs converge to a solution with very low cost that visually indistinguishable from the ground truth. A closer look at the results reveals that the runs that converge to a state with a high Young’s modulus reach a low value of stiffness damping, and vice versa.

These results illustrate that the optimization problem we solve is highly non-convex, and the optimizer can arrive at different solutions yielding equally good matches with the observations. This is a property our optimization approach shares with other non-linear optimization algorithms. As shown in the previous experiment, our algorithm typically successfully finds one of the possible solution. In

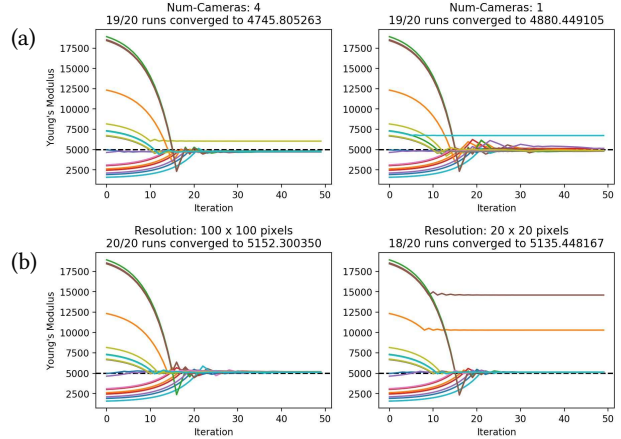


Fig. 10. Convergence behavior of our method towards a ground truth Young’s modulus of 5000 for different numbers of cameras (a) and resolutions of observed depth images (b). In (a), depth resolution was 50×50 , in (b), a single camera was used.

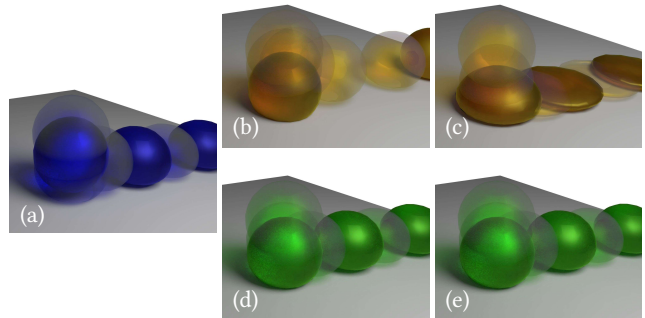


Fig. 11. Also when optimizing for multiple parameters at once, our algorithm can robustly reconstruct the ground truth motion (a), despite starting with very different initial conditions (b,c). For (b), the solid rendered frames indicate the different rolling behavior of the very stiff material in comparison to (a), while the very soft material in (c) leads to strong deformations. Our sparse surface constraints allow for a robust matching, that is visually indistinguishable from the ground truth, i.e. (d) reconstructed from (b), and (e) from (c). Quantified errors are given in the appendix.

practice, we alleviate this ambiguity by running a batch of optimizations with slightly perturbed initial conditions. Our cost function lets us reliably choose the best match from the batch, which we use as the final result. We employ this strategy in all of the following experiments.

7.4 Real-World Data

In addition to the synthetic test cases, we use three live captures of real-world objects to analyze the capabilities of our approach. The first test case is a plush teddy, of which a high-quality initial pose is obtained with a 3D scanner. An image sequence of the teddy falling onto the floor is then recorded with a commodity RGB-D

camera¹ (see Fig. 12a). Of this sequence, we use only the depth (D) channel as input for the optimizer (see Fig. 12b). From the initial configuration shown in Fig. 12c, the optimizer estimates gravity, the Young’s modulus, as well as the mass- and stiffness damping parameters.

Physical Units. The material estimates are performed in a virtual, unit-less coordinate system. To convert the estimated values to physical units, the simulated gravity needs to be scaled to relate the object’s size in the virtual space to its size in the real world. Furthermore, the object’s mass (the Young’s modulus depends on it) and the time step are required. Since the object’s mass cannot be recovered from the observations, we weight the objects beforehand. The time step is given by the known camera framerate of 60fps.

More specifically, we measure the size of the object S' in virtual meters m' via the signed distance function of the input ϕ_0 that defines the object in reference configuration Ω_r . Given the size of the object S in meters, we can compute the first scaling factor $f_{\text{size}} = S/S'$ in m/m' . Next, let M in kg be the mass of the real object. The parameter m in the physical model Eq. (1) specifies the mass density. Hence the virtual mass M' in kg' is given by $M' = mV$ where V is the object’s volume computed as $V = f_{\text{size}}^3 \int_{\Omega_r} 1 dx$. The scaling factor for the mass is then given as $f_{\text{mass}} = M/M'$ in kg/kg' . Last, we parametrize the simulation with the real-world time step, hence $f_{\text{time}} = 1s/1s'$. With these scaling factors, we can convert the value of the virtual Young’s modulus k (see Sec.3) into real-world units. The unit of the Young’s modulus is Pascal (kgm/s^2), hence the real-world value is given as $k \cdot f_{\text{mass}} f_{\text{size}} / f_{\text{time}}^2$. Similarly, let g be the reconstructed gravitational acceleration in virtual units. The real-world gravity is then given by $g \cdot f_{\text{size}} / f_{\text{time}}^2$.

Simulation Results. For our real-world cases, the accuracy of the estimated material parameters is affected by measurement noise as well as the non-physical damping distribution that is assumed in the simulation. Especially the latter introduces forces that reduce the gravity force, similar to an outer viscous medium [Adhikari and Phani 2004; Wilson 2002]. Similarly, since the soft collision model repulses the object already before the contact point is reached, it can require a stronger gravity force to compensate this effect. Hence, the estimated material parameters are typically less accurate than those obtained from more specialized laboratory experiments [Miguel et al. 2016; Zehnder et al. 2017].

The teddy was optimized for 50 iterations. Each iteration consists of a forward and adjoint simulation over 80 timesteps, and using 18 perturbed initial conditions. The plots of the single runs are shown in Figure 13. The best five runs exhibit large differences in the reconstructed values, while having an equally low cost. In the accompanying video, these five runs are compared side-by-side and closely match the bouncing behaviour of the teddy. The teddy, however, tilts to the side after the first bounce. We attribute this behaviour to inhomogeneities in the material composition, which cannot be reconstructed by our model. For the Young’s modulus, the initial value is several magnitudes higher than the reconstructed values of around 8, showing that the optimization is stable over a wide range of values. Furthermore, the stiffness and mass damping seem

Testcase	Teddy	Pillow-Flat	Pillow-Ramp
Run	14	8	7
Initial Cost	143.9	249.9	589.3
Recon. Cost	8.461	21.2	59.816
camera framerate	60Hz	60Hz	60 Hz
object size	0.33x0.22x0.18m	0.46x0.46x0.15m	0.46x0.46x0.15m
object mass	0.256kg	0.340kg	0.340kg
Gravity	$11.9 \frac{m}{s^2}$	$8.03 \frac{m}{s^2}$	$12.584 \frac{m}{s^2}$
Young’s Modulus	590Pa	151Pa	3430Pa
Mass Damping	0.240	0.078	0.068
Stiffness Damping	0.027	0.015	0.044
Ground Height	-	-	0.127m
Ground Theta	-	-	21.9°
Ground Phi	-	-	4.8°

Table 1. Input units and final reconstructions of real-world cases.

to be antimodal, i.e. a high value of mass damping is compensated to some extent by low stiffness damping, and vice versa.

For the best run, Table 1 shows the reconstructed values with physical units if possible, and for the 5 best runs Table 3 gives the recorded parameter values of the simulation. The initial configuration and the reconstructed configuration for the best run is shown in Figure 12c and Figure 12d, respectively. As one can see, the gravity is slightly off from the ground truth of $9.81 \frac{m}{s^2}$, possibly due to the Rayleigh damping. The reconstructed value of 590Pa is around five times softer than e.g. polystyrene foam of ca. 2500Pa. This is a plausible value since from the bouncing behavior, the teddy is softer than typical polystyrene foam.

We also reconstruct a pillow falling onto a flat floor. We let the optimizer simultaneously reconstruct gravity, Young’s modulus, mass- and stiffness damping parameters, with 15 perturbed initial configurations. Our method finds a plausible match for the complex deformations of the pillow, the details for which can be found in the accompanying video and in Appendix D, the reconstructed values for the best run can be found in Table 1.

Last, we recorded the pillow falling onto a ramp and bouncing off, in order to let our algorithm reconstruct the object as well as the collision geometry. The recorded RGB-D sequence is shown in Fig. 14a and Fig. 14b. We let the optimizer simultaneously reconstruct gravity, Young’s modulus, mass- and stiffness damping parameters, the ground plane height, as well as the three degrees of freedom of the ground plane orientation, with 20 perturbed initial configurations. Our method recovers both a plausible orientation of the ramp and the object’s material parameters purely from the sequence of depth images. To our knowledge, this is the first simultaneous physical reconstruction of a deformable object and its environment from a single depth video. Since we compute collisions against a single plane, only the tilted ramp is reconstructed while the second collision with the flat table is ignored. Furthermore, since we do not consider friction in the underlying physical model, the simulation cannot accurately match the speed of the sliding pillow. This is a challenging test case for our method, as indicated by the plots in Figure 15. The parametric ambiguities, e.g. the same contact point can be obtained with higher and steep or low and flat ground planes, lead to noticeable differences in the reconstructions. The

¹An Asus Xtion ProLive camera.

	Dragon	Torus	Ball	Teddy	Pillow-Fl.	Pillow-R.
# active nodes	2489	1138	770	2440	3836	4390
# elements	1562	690	516	1716	2848	3284
# diffused nodes	11587	4670	2605	14612	19006	21530
# timesteps	10	40	20	100	450	175
# cameras	1	1	1	1	1	1
Camera res.	50x50	50x50	50x50	320x240	320x240	320x240
Obs. n 'th	1	1	1	5	5	5
ϕ_{\max}	4	5	2	10	10	10
# ini. cond.	2	20	20-60	18	10	15
Forw. sim. (s)	0.318	0.095	0.077	0.803	0.240	0.264
Cost eval. (s)	0.172	0.092	0.199	0.165	0.085	0.153
Adj. sim. (s)	0.462	0.225	0.058	0.764	0.213	0.292
# iter. steps	50	100	30	50	50	50

Table 2. Timing and model statistics for different test cases. Timings are per timestep. Dragon, Torus and Ball are synthetic datasets, Teddy, Pillow-Flat and Pillow-Ramp refer to real-world scans. "Obs. n 'th" denotes the interval in simulation steps between observations, while "Ini. cond." denotes the number of randomly perturbed initial conditions used for the optimization.

difficult setup of the ramp test case also leads to material estimates in Table 1 which indicate that our models tries to compensate for the missing physical phenomena by increasing the material stiffness significantly. Nonetheless, our final result yields a realistic reconstruction of the initial impact and still partially matches the observed sliding behavior.

Timings. Performance details for our solver and optimization are given in Table 2. Overall, our forward solve is very fast, with less than one second per timestep for all our examples. The backward pass typically takes a similar time, resulting in a total runtime of e.g. around 40 minutes for the teddy.

8 OUTLOOK AND LIMITATIONS

We see our novel formulation for gradient-based inverse parameter estimation using sparse constraints and physical priors as an important step toward more reliable object reconstruction. There is huge potential for computer vision tasks to improve unseen or occluded motion, such as the backside of an object, via physical priors. It will also be particularly interesting to investigate the incorporation of soft body physics into deep learning methods via our differentiable formulation. By shifting the workload to a physics-based training process it is potentially possible to train neural networks in a fully or partially unsupervised manner.

It should also be noted that our approach comes with some limitations and restrictions. In contrast to previous work [Wang et al. 2015] we require an initial object pose. It would be highly interesting to combine our method with the rest pose estimation proposed there. In our current approach we consider the extension region only in proximity to the domain covered by the object. Thus, the cost function cannot be evaluated at points that are observed far outside this region. To handle such cases, it will be interesting to investigate multi-scale approaches that can efficiently propagate deformations into a wider region around the object. As our algorithm can arrive at multiple solutions with different parameter values, we are also interested in decreasing these ambiguities by introducing additional priors or domain-specific knowledge about the observed materials.

In addition, it will be a very interesting and fruitful direction for future work to improve the physical models to account, e.g., for friction. To incorporate such effects, it is necessary to include more physical accurate collision solvers using, e.g., using Linear Complementary Problems [Anitescu and Potra 1997; Foutayenia et al. 2014; Mordatch et al. 2012]. More flexible and realistic material models, such as the Neo-Hookean model [Smith et al. 2018], would also be highly interesting additions.

9 CONCLUSION

We have proposed a framework to infer an elastic simulation of a deformable object directly from a sparse set of depth images obtained from one or more cameras. To this end, we coupled a finite-element elasticity simulation framework with the depth sensor measurements via a loss function that imposes sparse surface constraints. In this way we can infer plausible elastic simulation parameters, even those for collision geometry, from a very limited number of observations — for example a single stream of depth images. All parameters of the simulation are inferred directly by first-order optimization algorithms applied in a hybrid Lagrangian-Eulerian formulation. We have validated our method quantitatively and qualitatively on a variety of simulated and real observations. In addition, we have demonstrated that our method can robustly recover complex material behavior in real-world scenarios.

REFERENCES

- Sondipon Adhikari and A Srikantha Phani. 2004. Rayleigh's Classical Damping Revisited. (2004).
- M. Anitescu and F. A. Potra. 1997. Formulating Dynamic Multi-Rigid-Body Contact Problems with Friction as Solvable Linear Complementarity Problems. *Nonlinear Dynamics* 14 (1997), 231–247.
- Jernej Barbič and Doug L James. 2005. Real-time subspace integration for St. Venant-Kirchhoff deformable models. *ACM transactions on graphics (TOG)* 24, 3 (2005), 982–990.
- Jernej Barbič, Marco da Silva, and Jovan Popović. 2009. Deformable object animation using reduced optimal control. *ACM Transactions on Graphics* 28, 3 (2009), 1. <https://doi.org/10.1145/1531326.1531359>
- Jernej Barbič, Funshing Sin, and Eitan Grinspun. 2012. Interactive editing of deformable simulations. *ACM Transactions on Graphics* 31, 4 (2012), 1–8. <https://doi.org/10.1145/2185520.2185566>
- T. Belytschko and T. Black. 1999. Elastic crack growth in finite elements with minimal remeshing. *Internat. J. Numer. Methods Engrg.* 45 (June 1999), 601–620. [https://doi.org/10.1002/\(SICI\)1097-0207\(19990620\)45:5<601::AID-NME598>3.0.CO;2-S](https://doi.org/10.1002/(SICI)1097-0207(19990620)45:5<601::AID-NME598>3.0.CO;2-S)
- J. Benk, M. Ulbrich, and M. Mehl. 2012. The Nitsche Method of the Navier-Stokes Equations for Immersed Boundaries. In *Seventh International Conference on Computation Fluid Dynamics (ICCFD7)*.
- Miklós Bergou, Saurabh Mathur, Max Wardetzky, and Eitan Grinspun. 2007. TRACKS: Toward Directable Thin Shells. *ACM Transactions on Graphics* 26, 99 (2007), 50. <https://doi.org/10.1145/1239451.1239501>
- Bernd Bickel, Moritz Bächer, Miguel A. Otaduy, Hyunho Richard Lee, Hanspeter Pfister, Markus Gross, and Wojciech Matusik. 2010. Design and Fabrication of Materials with Desired Deformation Behavior. In *ACM SIGGRAPH 2010 Papers (SIGGRAPH '10)*. ACM, Article 63, 10 pages. <https://doi.org/10.1145/1833349.1778800>
- Bernd Bickel, Moritz Bächer, Miguel A Otaduy, Wojciech Matusik, Hanspeter Pfister, and Markus Gross. 2009. Capture and modeling of non-linear heterogeneous soft tissue. In *ACM Transactions on Graphics (TOG)*, Vol. 28(3). ACM, 89.
- Christopher Brandt, Elmar Eisemann, and Klaus Hildebrandt. 2018. Hyper-reduced projective dynamics. *ACM Transactions on Graphics (TOG)* 37, 4 (2018), 80.
- Robert Bridson, Ronald Fedkiw, and John Anderson. 2002. Robust Treatment of Collisions, Contact and Friction for Cloth Animation. *Proc. Conf. Computer Graphics and Interactive Techniques* (2002), 594–603. <https://doi.org/10.1145/566570.566623>
- Bridson, R. 2015. *Fluid simulation for computer graphics*. AK Peters/CRC Press.
- Richard H. Byrd, Peihuang Lu, Jorge Nocedal, and Ciyu Zhu. 1995. A Limited Memory Algorithm for Bound Constrained Optimization. *SIAM Journal on Scientific Computing* 16, 5 (1995), 1190–1208. <https://doi.org/10.1137/0916069> arXiv:<https://doi.org/10.1137/0916069>

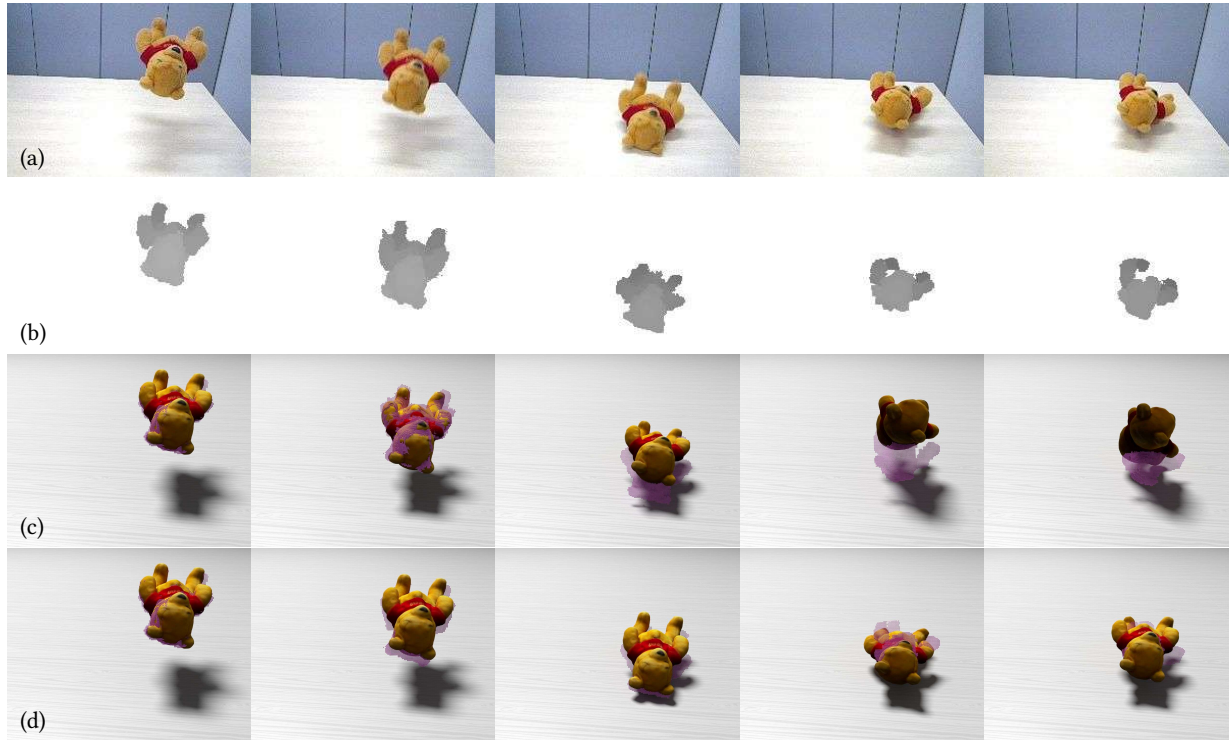


Fig. 12. From top to bottom: Observed colors, observed depths, initial configuration, reconstructed model (purple dots indicate observations). Each row shows a sequence of steps over time.

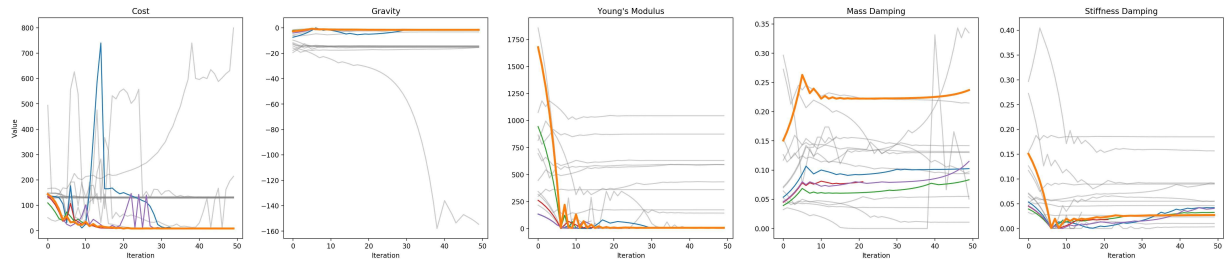


Fig. 13. Convergence plots for teddy, using 18 randomly selected initial parameter sets. Plots of best 5 runs drawn in color, plot of best run thickened.

Desai Chen, David IW Levin, Shinjiro Sueda, and Wojciech Matusik. 2015. Data-driven finite elements for geometry and material design. *ACM Transactions on Graphics (TOG)* 34, 4 (2015), 74.

Xiang Chen, Changxi Zheng, Weiwei Xu, and Kun Zhou. 2014. An asymptotic numerical method for inverse elastic shape design. *ACM Transactions on Graphics* 33, 4 (2014), 1–11. <https://doi.org/10.1145/2601097.2601189>

Min Gyu Choi and Hyeong-Seok Ko. 2005. Modal warping: Real-time simulation of large rotational deformation and manipulation. *IEEE Transactions on Visualization and Computer Graphics* 11, 1 (2005), 91–101.

John. D. Cook. 2010. Soft maximum function. <https://www.johndcook.com/blog/2010/01/13/soft-maximum/>. (2010). Accessed 07/26/2018.

Stelian Coros, Sebastian Martin, Bernhard Thomaszewski, Christian Schumacher, Robert Sumner, and Markus Gross. 2012. Deformable objects alive! *ACM Transactions on Graphics* 31, 4 (2012), 1–9. <https://doi.org/10.1145/2185520.2185565>

Edilson de Aguiar, Carsten Stoll, Christian Theobalt, Naveed Ahmed, Hans-Peter Seidel, and Sebastian Thrun. 2008. Performance Capture from Sparse Multi-view Video. *ACM Trans. Graph.* 27, 3, Article 98 (Aug. 2008), 10 pages. <https://doi.org/10.1145/1360612.1360697>

Christian Dick. 10.01.2012. *Computational Steering for Implant Planning in Orthopedics*. Dissertation. Technische Universität München, München.

Christian Dick, Joachim Georgii, and Rüdiger Westermann. 2011. A Real-Time Multi-grid Finite Hexahedra Method for Elasticity Simulation using CUDA. *Simulation Modelling Practice and Theory* 19, 2 (2011), 801–816.

Florian Ferstl, Rüdiger Westermann, and Christian Dick. 2014. Large-Scale Liquid Simulation on Adaptive Hexahedral Grids. *Visualization and Computer Graphics, IEEE Transactions on* 20, 10 (Oct 2014), 1405–1417. <https://doi.org/10.1109/TVCG.2014.2307873>

Roger Fletcher. 2005. On the Barzilai-Borwein Method. In *Optimization and Control with Applications*, Liqun Qi, Koklay Teo, and Xiaoqi Yang (Eds.). Springer US, Boston, MA, 235–256.

Y. El Foutayenia, H. El Bouananib, and M. M. Khaladic. 2014. The Linear Complementarity Problem and a Method to find all its solutions. *Information in Sciences and Computing* 3 (2014).

Thomas Peter Fries and Ted Belytschko. 2010. The extended/generalized finite element method. *International journal for numerical methods in engineering* 84, 3 (15 10 2010), 253–304. <https://doi.org/10.1002/nme.2904>

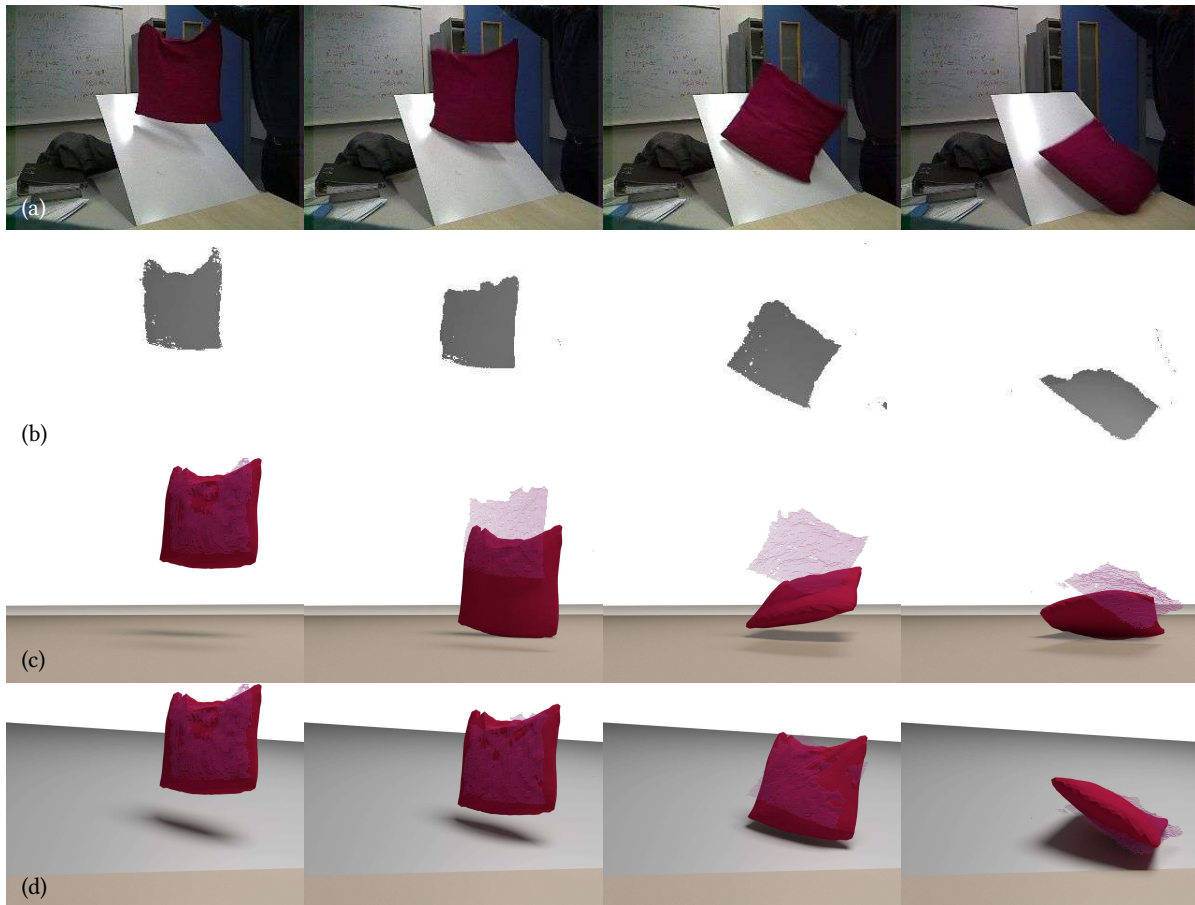


Fig. 14. From top to bottom: Observed colors, observed depths, initial configuration, reconstructed model (purple dots indicate observations). Each row shows a sequence of steps over time.

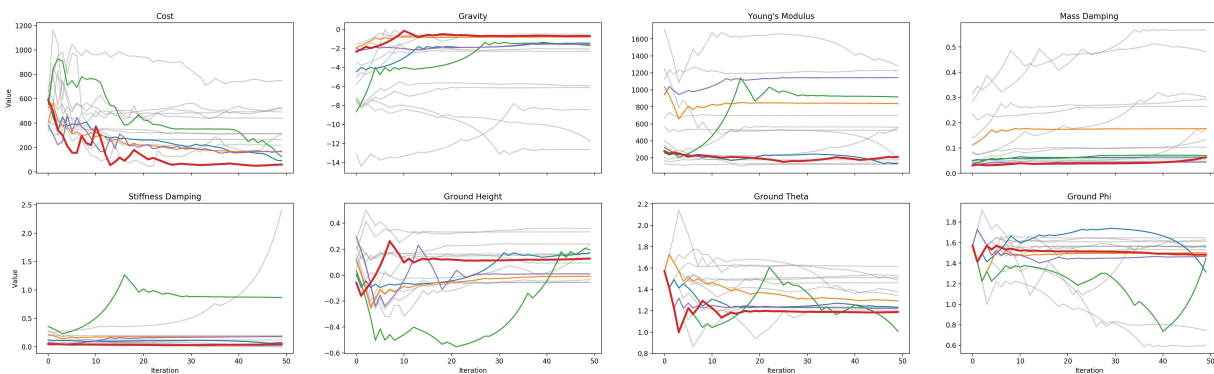


Fig. 15. Convergence plots for pillow, using 18 randomly selected initial parameter sets. Plots of best 5 runs drawn in color, plot of best run thickened.

Joachim Georgii and Rüdiger Westermann. 2008. Corotated Finite Elements Made Fast and Stable. In *VRIPHYS*.
 Nachiket H Gokhale, Paul E Barbone, and Assad A Oberai. 2008. Solution of the nonlinear elasticity imaging inverse problem: the compressible case. *Inverse Problems* 24, 4 (2008), 045010. <https://doi.org/10.1088/0266-5611/24/4/045010>

Chris Greenough. 2001. Newmark's Method of Direct Integration. <http://www.softeng.rl.ac.uk/st/projects/felib3/Docs/html/Intro/intro-node52.html>. (2001). Accessed: 05/17/2018.
 Peter Hansbo, Mats G. Larson, and Sara Zahedi. 2014. A cut finite element method for a Stokes interface problem. *Applied Numerical Mathematics* 85 (2014), 90 – 114. <https://doi.org/10.1016/j.apnum.2014.06.009>

- Michael Hauth and Wolfgang Strasser. 2003. Corotational Simulation of Deformable Solids. *Journal of WSCG* 12, 1-3 (2003).
- Matthias Innmann, Michael Zollhöfer, Matthias Niessner, Christian Theobald, and Marc Stamminger. 2016. VolumeDeform: Real-Time Volumetric Non-rigid Reconstruction. In *ECCV 2016*. Lecture Notes in Computer Science, Vol. 9912. Springer International Publishing, Cham, 362–379. https://doi.org/10.1007/978-3-319-46484-8_122
- Mika Juntunen and Rolf Stenberg. 2009. Nitsche's method for general boundary conditions. *Math. Comp.* 78, 267 (2009), 1353–1374. <https://doi.org/10.1090/S0025-5718-08-02183-2>
- Meekyoung Kim, Gerard Pons-Moll, Sergi Pujades, Seungbae Bang, Jinwook Kim, Michael J. Black, and Sung-Hee Lee. 2017. Data-driven physics for human soft tissue animation. *ACM Transactions on Graphics* 36, 4 (2017), 1–12. <https://doi.org/10.1145/3072959.3073685>
- Dan Koschier, Jan Bender, and Nils Thuerey. 2017. Robust eXtended Finite Elements for Complex Cutting of Deformables. *ACM Transactions on Graphics* 36, 4 (2017), 55:1–55:13.
- Martin Kroon and Gerhard A Holzapfel. 2008. Estimation of the distributions of anisotropic , elastic properties and wall stresses of saccular cerebral aneurysms by inverse analysis. In *Proceedings of the Royal Society A: Mathematical, Physical and Engineering Sciences*.
- Tassilo Kugelstadt, Dan Koschier, and Jan Bender. 2018. Fast Corotated FEM using Operator Splitting. *Computer Graphics Forum (SCA)* 37, 8 (2018).
- Hao Li, Bart Adams, Leonidas J Guibas, and Mark Pauly. 2009. Robust single-view geometry and motion reconstruction. *ACM Transactions on Graphics (TOG)* 28, 5 (2009), 175.
- Ran Luo, Tianjia Shao, Huamin Wang, Weiwei Xu, Kun Zhou, and Yin Yang. 2018. DeepWarp: DNN-based Nonlinear Deformation. *arXiv preprint arXiv:1803.09109* (2018).
- Mickaël Ly, Romain Casati, Florence Bertails-Descoubes, Mélina Skouras, and Laurence Boissieux. 2018. Inverse elastic shell design with contact and friction. In *SIGGRAPH Asia 2018 Technical Papers*. ACM, 201.
- Martin Mächler. 2012. Accurately Computing $\log(1 - \exp(\cdot))$. (2012). <https://cran.r-project.org/web/packages/Rmpfr/vignettes/log1mexp-note.pdf>
- Antoine McNamara, Adrien Treuille, Zoran Popović, and Jos Stam. 2004. Fluid Control Using the Adjoint Method. *ACM Trans. Graph.* 23, 3 (Aug. 2004), 449–456. <https://doi.org/10.1145/1015706.1015744>
- Eder Miguel, David Miraut, and Miguel A Otaduy. 2016. Modeling and Estimation of Energy-Based Hyperelastic Objects. In *Computer Graphics Forum*, Vol. 35(2). Wiley Online Library, 385–396.
- Rajat Mittal and Gianluca Iaccarino. 2005. Immersed Boundary Methods. *Annual Review of Fluid Mechanics* 37, 1 (2005), 239–261. <https://doi.org/10.1146/annurev.fluid.37.061903.175743>
- Aron Monzspart, Nils Thuerey, and Niloy J Mitra. 2016. SMASH: Data-driven Reconstruction of Physically Valid Collisions. *CM Transactions on Graphics (TOG)* 35, 6 (2016).
- Igor Mordatch, Emanuel Todorov, and Zoran Popović. 2012. Discovery of complex behaviors through contact-invariant optimization. *ACM Transactions on Graphics* 31, 4 (2012), 1–8. <https://doi.org/10.1145/2185520.2185539>
- Matthias Müller, Julie Dorsey, Leonard McMillan, Robert Jagnow, and Barbara Cutler. 2002. Stable real-time deformations. In *Proceedings of the 2002 ACM SIGGRAPH/Eurographics symposium on Computer animation*. ACM, 49–54.
- Stanley Osher and Ronald Fedkiw. 2006. *Level set methods and dynamic implicit surfaces*. Vol. 153. Springer Science & Business Media.
- Zherong Pan, Hujun Bao, and Jin Huang. 2015. Subspace dynamic simulation using rotation-strain coordinates. *ACM Transactions on Graphics (TOG)* 34, 6 (2015), 242.
- Zherong Pan and Dinesh Manocha. 2018. Active Animations of Reduced Deformable Models with Environment Interactions. *ACM Transactions on Graphics (TOG)* 37, 3 (2018), 36.
- Yuri Pekelny and Craig Gotsman. 2008. Articulated object reconstruction and markerless motion capture from depth video. In *Computer Graphics Forum*, Vol. 27(2). Wiley Online Library, 399–408.
- Qiuv, Y. 2016. LBFGSpp. <https://github.com/yixuan/LBFGSpp>. (2016).
- Martin Riedmiller and Heinrich Braun. 1993. A direct adaptive method for faster backpropagation learning: The RPROP algorithm. In *Neural Networks, 1993., IEEE International Conference on*. IEEE, 586–591.
- Petter Risholm, James Ross, George R. Washko, and William Wells. 2011. Probabilistic elastography estimating lung elasticity. *Inf. Process Med. Imaging* (2011), 699–710.
- John Schulman, Alex Lee, Jonathan Ho, and Pieter Abbeel. 2013. Tracking deformable objects with point clouds. In *Proceedings - IEEE International Conference on Robotics and Automation*. 1130–1137.
- Kristian Schulz, Christoph von Tycowicz, Hans-Peter Seidel, and Klaus Hildebrandt. 2014. Animating deformable objects using sparse spacetime constraints. *ACM Transactions on Graphics* 33, 4 (2014), 1–10. <https://doi.org/10.1145/2601097.2601156>
- Ken Shoemake and Tom Duff. 1992. Matrix animation and polar decomposition. In *Proceedings of the conference on Graphics interface*, Vol. 92. 258–264.
- Eftychios Sifakis and Jernej Barbič. 2015. Finite Element Method Simulation of 3D Deformable Solids. *Synthesis Lectures on Visual Computing: Computer Graphics, Animation, Computational Photography, and Imaging* 1, 1 (2015), 1–69.
- Eftychios D. Sifakis. 2012. FEM Simulation of 3D Deformable Solids: A practitioner's guide to theory, discretization and model reduction: Part One: The classical FEM method and discretization methodology. (2012). <http://www.femdefo.org/>
- Miroslava Slavcheva, Maximilian Baust, Daniel Cremers, and Slobodan Ilic. 2017. Killing-fusion: Non-rigid 3d reconstruction without correspondences. In *Proceedings of the IEEE Conference on Computer Vision and Pattern Recognition*. 1386–1395.
- Breannan Smith, Fernando De Goes, and Theodore Kim. 2018. Stable Neo-Hookean Flesh Simulation. *ACM Transactions on Graphics (TOG)* 37, 2 (2018), 12.
- Bin Wang, Paul G. Kry, Yuanmin Deng, Uri M. Ascher, Hui Huang, and Baoquan Chen. 2018. Neural Material: Learning Elastic Constitutive Material and Damping Models from Sparse Data. *arXiv 1808.04931* (2018).
- Bin Wang, Longhua Wu, KangKang Yin, Uri Ascher, Libin Liu, and Hui Huang. 2015. Deformation capture and modeling of soft objects. *ACM Transactions on Graphics (TOG)* 34, 4 (2015), 94.
- Huamin Wang, James F O'Brien, and Ravi Ramamoorthi. 2011. Data-driven elastic models for cloth: modeling and measurement. In *ACM Transactions on Graphics (TOG)*, Vol. 30(4). ACM, 71.
- Weiss, S. 2018. cuMat. <https://gitlab.com/shaman42/cuMat>. (2018).
- Edward L Wilson. 2002. Three-dimensional static and dynamic analysis of structures. (2002).
- Jun Wu, Rüdiger Westermann, and Christian Dick. 2015. A Survey of Physically Based Simulation of Cuts in Deformable Bodies. *Computer Graphics Forum* 34, 6 (2015), 161–187. <https://doi.org/10.1111/cgf.12528>
- Hongyi Xu, Yijing Li, Yong Chen, and Jernej Barbič. 2015. Interactive material design using model reduction. *ACM Transactions on Graphics (TOG)* 34, 2 (2015), 18.
- Hongyi Xu, Yili Zhao, and Jernej Barbič. 2014. Implicit multibody penalty-based distributed contact. *IEEE Transactions on Visualization & Computer Graphics* 9 (2014), 1266–1279.
- Yin Yang, Dingzeyu Li, Weiwei Xu, Yuan Tian, and Changxi Zheng. 2015. Expediting precomputation for reduced deformable simulation. *ACM Transactions on graphics (TOG)* 34, 6 (2015).
- Yin Yang, Weiwei Xu, Xiaohu Guo, Kun Zhou, and Baining Guo. 2013. Boundary-aware multidomain subspace deformation. *IEEE transactions on visualization and computer graphics* 19, 10 (2013), 1633–1645.
- Jonas Zehnder, Espen Knoop, Moritz Bächer, and Bernhard Thomaszewski. 2017. Metasilicone: design and fabrication of composite silicone with desired mechanical properties. *ACM Transactions on Graphics (TOG)* 36, 6 (2017), 240.
- Qingyu Zhao, Stephen Pizer, Ron Alterovitz, and Marc Niethammer. 2017. Orthotropic Thin Shell Elasticity Estimation for Surface Registration. In *Information Processing in Medical Imaging*. Lecture Notes in C. S., Vol. 10265. Springer Intl. Publishing, Cham, 493–504. https://doi.org/10.1007/978-3-319-59050-9_39

Supplemental Material - Appendix

A PHYSICS SIMULATION

In the following, we detail the physical model and governing equations underlying our work, and we describe the particular discretization scheme used.

Strong Form. Let the reference configuration be given in Ω^r . The displacement at time t is given by $u : \Omega^r \times t \rightarrow \mathbb{R}^3$. Then the linear Green strain tensor is given by

$$E(u) := \frac{1}{2} (\nabla u + (\nabla u)^T) \in \mathbb{R}^{3 \times 3} \quad (20)$$

and the Piola-Kirchoff stress tensor

$$P(u) := 2\mu E(u) + \lambda \text{tr}(E(u)) \mathbf{1} \quad (21)$$

with the Lamé coefficients μ and λ derived from the Young's modulus k and the Poisson ratio ρ . The dynamic elasticity problem in strong form is then defined as

$$m\ddot{u} - \text{div} P(u) = f_B \text{ in } \Omega^r \times \mathbb{R}_0^+ \quad (22a)$$

$$u = u_D \text{ on } \Gamma_D^r \times \mathbb{R}_0^+ \quad (22b)$$

$$P(u) \cdot \mathbf{n} = f_S \text{ in } \Gamma_N^r \times \mathbb{R}_0^+ \quad (22c)$$

$$u = u^0 \text{ in } \Omega^r \times \{0\} \quad (22d)$$

$$\dot{u} = \dot{u}^0 \text{ in } \Omega^r \times \{0\}, \quad (22e)$$

with the mass m , Dirichlet boundaries Γ_D^r and Neumann boundaries Γ_N^r .

Weak Form. To obtain the weak form, let $V := H^1(\bar{\Omega}^r \rightarrow \mathbb{R}^d)$ be the space of test and trial functions. Because Neumann and Dirichlet boundaries are enforced weakly, the space of test and trial functions coincide. Starting from the right hand side of Eq. (22a), the generalized divergence theorem yields:

$$\begin{aligned} \int_{\Omega} f_B \cdot v \, dx &= \int_{\Omega} -\text{div} P(u) \cdot v \, dx \\ &= \int_{\Omega} \sum_{j=1}^d \left(\mu \left(\nabla u_j + \frac{\partial}{\partial x_j} u \right) + \lambda \sum_{i=1}^d \frac{\partial u_i}{\partial u_j} \mathbf{1}_j \right) \cdot \nabla v_j \, dx \\ &\quad - \int_{\partial\Omega} \sum_{j=1}^d \left(\mu \left(\nabla u_j + \frac{\partial}{\partial x_j} u \right) \right. \\ &\quad \left. + \lambda \sum_{i=1}^d \frac{\partial u_i}{\partial u_j} \mathbf{1}_j \right) \cdot \mathbf{n} v_j \, ds + \int_{\Omega} m \ddot{u} v \, dx. \end{aligned} \quad (23)$$

A.1 Hexahedral Finite Element Discretization

Trilinear shape functions are assigned to the finite hexahedral elements (see Fig. 16).

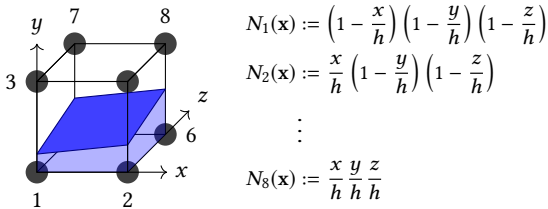


Fig. 16. Trilinear hexahedral element and embedded surface

Thus, inside a cell, any function f can be approximated by trilinear interpolation of its values at the eight corners \mathbf{v}_i as

$$f(\mathbf{x}) \approx \sum_{i=1}^8 f(\mathbf{v}_i) N_i(\mathbf{x}). \quad (24)$$

Partially Filled Cells. We further embed the object boundary into the simulation grid, and consider cells that are partly filled with material. For cells of size $[0, 1]^3$, and the object given as signed distance function ϕ , we define the part of a cell that is contained in the object as

$$\Omega^e := \{\mathbf{x} \in [0, 1]^3 : \phi(\mathbf{x}) \leq 1\}. \quad (25)$$

For a trilinear interpolation within cells, integrals of arbitrary functions over cells can be approximated as

$$\int_{\Omega^e} f(x) \, dx \approx \int_{\Omega^e} \sum_{i=1}^8 f(\mathbf{v}_i) N_i(x) \, dx = \sum_{i=1}^8 f(\mathbf{v}_i) \underbrace{\int_{\Omega^e} N_i(x) \, dx}_{=: w_{\nu}(e, i)} \quad (26)$$

where the integrals of the basis functions w_{ν} are precomputed and stored per cell. As cell vertices do not necessarily lie on the object surface, we use Nitsche's method [Benk et al. 2012; Juntunen and Stenberg 2009] to incorporate Dirichlet boundaries.

Discrete Equations. With the basis functions from Eq. (26) we arrive at the following per-cell expressions:

$$M^e = \int_{\Omega^e} \Phi^e(x)^T m \Phi^e(x) \, dx \in \mathbb{R}^{24 \times 24} \quad (27)$$

$$K^e = \int_{\Omega^e} B^e(x)^T C B^e(x) \, dx \in \mathbb{R}^{24 \times 24} \quad (28)$$

$$f^e = \int_{\Gamma_N^e} \Phi^e(s)^T \mathbf{f}_S(s) \, ds \in \mathbb{R}^{24} \quad (29)$$

Here, $\Phi^e(x) \in \mathbb{R}^{3 \times 24}$ and $B^e(x) \in \mathbb{R}^{6 \times 24}$, respectively, store for each coordinate the values of the basis functions N_i and the derivatives. $C \in \mathbb{R}^{6 \times 6}$ is the regular material matrix for the chosen Lamé coefficients.

Corotation. To handle large rotations, we utilize the corotation formulation [Dick 2012; Dick et al. 2011; Georgii and Westermann 2008; Hauth and Strasser 2003; Sifakis 2012]. First, the rotational part R^e of the deformation of cell e is extracted. Let the average deformation gradient F^e be computed as [Georgii and Westermann 2008]

$$F^e = \mathbf{1}_3 + \frac{1}{4h} \sum_{i=1}^8 \mathbf{u}_{S(e, i)} \begin{pmatrix} (-1)^i \\ (-1)^{\lceil i/2 \rceil} \\ (-1)^{\lceil i/4 \rceil} \end{pmatrix}^T. \quad (30)$$

The rotational component R^e is then given by the polar decomposition $F^e = R^e S^e$ and can be computed with iterative procedures [Hauth and Strasser 2003; Shoemake and Duff 1992]. If the polar decomposition should also handle flipped elements and inversions correctly, a more robust, but also more expensive Analytic Polar Decomposition [Kugelstadt et al. 2018] would be needed (not used in this work). Second, given R^e , the per-element term $K^e \underline{\mathbf{u}}^e$ is replaced by

$$T^e K^e ((R^e)^T (\underline{\mathbf{x}}^e + \underline{\mathbf{u}}^e) - \underline{\mathbf{x}}^e). \quad (31)$$

A.2 Blocked Expressions for Matrix Assembly

One advantage of our chosen discretization is that the per-element stiffness matrix K^e (Eq. (27)) has a 3×3 block structure that is highly amenable to optimized implementations. Each block describes the interactions between the coordinates of the two corresponding cell nodes. Modulo index variations, the computation of these 3×3 blocks is identical for all 64 blocks. Furthermore, the corotational strain formulation and Nitsche Dirichlet boundaries can be incorporated into the block-wise decomposition in a straight forward way.

The regular block structure facilitates storing the stiffness matrix K in a blocked compressed-sparse-row (CSR) format. During assembly, work groups can process a single cell in parallel. Reductions within the cell, as needed, e.g., for the computation of corotations and gradients, can be performed efficiently with warp-reductions. By including analytic simplifications of the basis function evaluations (and their derivatives), we arrive at a highly GPU-friendly algorithm that yields excellent performance.

The evaluation of the per-element stiffness matrix K^e is performed blockwise. Each of the 8×8 blocks $K_{i,j}^e \in \mathbb{R}^{3 \times 3}$ are computed in parallel. Let $\frac{\partial N_i(x_c)}{\partial x_j}$ be the derivatives of the basis functions at the eight cell corner. This $8 \times 8 \times 3$ table only contains the entries $-\frac{1}{h}$, 0 or $\frac{1}{h}$. It is stored in constant memory on the GPU and hence allows fast access via the cache. The per-block expression for the stiffness matrix K^e , see Eq. (28) for the definition, is given by:

$$K_{i,j}(x) = \begin{bmatrix} (2\mu + \lambda) \frac{\partial N_i(x)}{\partial x_1} \frac{\partial N_j(x)}{\partial x_1} + \mu \left(\frac{\partial N_i(x)}{\partial x_2} \frac{\partial N_j(x)}{\partial x_2} + \frac{\partial N_i(x)}{\partial x_3} \frac{\partial N_j(x)}{\partial x_3} \right) \\ \mu \frac{\partial N_i(x)}{\partial x_1} \frac{\partial N_j(x)}{\partial x_2} + \lambda \frac{\partial N_i(x)}{\partial x_2} \frac{\partial N_j(x)}{\partial x_1} \\ \mu \frac{\partial N_i(x)}{\partial x_1} \frac{\partial N_j(x)}{\partial x_3} + \lambda \frac{\partial N_i(x)}{\partial x_3} \frac{\partial N_j(x)}{\partial x_1} \\ (2\mu + \lambda) \frac{\partial N_i(x)}{\partial x_2} \frac{\partial N_j(x)}{\partial x_2} + \mu \left(\frac{\partial N_i(x)}{\partial x_1} \frac{\partial N_j(x)}{\partial x_1} + \frac{\partial N_i(x)}{\partial x_3} \frac{\partial N_j(x)}{\partial x_3} \right) \\ \mu \frac{\partial N_i(x)}{\partial x_2} \frac{\partial N_j(x)}{\partial x_3} + \lambda \frac{\partial N_i(x)}{\partial x_3} \frac{\partial N_j(x)}{\partial x_2} \\ \mu \frac{\partial N_i(x)}{\partial x_3} \frac{\partial N_j(x)}{\partial x_3} + \lambda \frac{\partial N_i(x)}{\partial x_1} \frac{\partial N_j(x)}{\partial x_1} \\ (2\mu + \lambda) \frac{\partial N_i(x)}{\partial x_3} \frac{\partial N_j(x)}{\partial x_3} + \mu \left(\frac{\partial N_i(x)}{\partial x_1} \frac{\partial N_j(x)}{\partial x_1} + \frac{\partial N_i(x)}{\partial x_2} \frac{\partial N_j(x)}{\partial x_2} \right) \end{bmatrix}. \quad (32)$$

A.3 Nitsche Dirichlet Boundaries

To incorporate Dirichlet boundaries with Nitsche's method, the weak form from Eq. 27 is extended using productive zeros $u - u_0$:

$$- \int_{\Gamma_N^r} P(u) \cdot n \cdot v \, ds - \int_{\Gamma_N^r} P(v) \cdot n \cdot (u - u_0) \, ds - \eta \int_{\Gamma_N^r} (u - u_0) \cdot v \, ds. \quad (33)$$

The first term makes the resulting linear system symmetric. The second term enforces the Dirichlet boundaries. The third term acts as a regularizer and the parameter η has to be chosen as $\eta \geq ch^{-1}$ with h being the grid size and c a sufficient large constant. In our experiments, we chose 10^8 for stable results.

These boundary conditions can also be formulated in an efficient, blocked matrix form. First, the definition of $P(u)$ (Eq. (21)) is used,

leading to the following terms that are added to the weak form (Eq. (23)):

$$\begin{aligned} & - \underbrace{\int_{\Gamma_D^e} \sum_{j=1}^3 \left(\mu \left(\nabla u_j \cdot n + \frac{\partial u}{\partial x_j} \cdot n \right) + \lambda n_j \sum_{i=1}^3 \frac{\partial u_i}{\partial x_i} \right) v_j \, ds}_{(I)} \\ & - \underbrace{\int_{\Gamma_D^e} \sum_{j=1}^3 \left(\mu \left(\nabla v_j \cdot n + \frac{\partial v}{\partial x_j} \cdot n \right) + \lambda n_j \sum_{i=1}^3 \frac{\partial v_i}{\partial x_i} \right) u_j \, ds}_{(I')} \\ & - \underbrace{\eta \int_{\Gamma_D^e} u \cdot v \, ds}_{(II)} \end{aligned} \quad (34)$$

Expressing u and v using the basis functions and their derivatives, combined in Φ^e and B^e , we obtain

$$K^e = - \int_{\Gamma_D^e} \Phi^e(x)^T D^e B^e(x) \, ds \quad (35)$$

for (34.I) with D^e given by

$$D^e := \begin{pmatrix} 2\mu n_1 + \lambda n_1 & \lambda n_1 & \lambda n_1 \\ \lambda n_2 & 2\mu n_2 + \lambda n_2 & \lambda n_2 \\ \lambda n_3 & \lambda n_3 & 2\mu n_3 + \lambda n_3 \end{pmatrix}. \quad (36)$$

Here, the equation for (34.I') is the above equation, just transposed. This integral is evaluated by computing the sum of the values at the eight corners weighted by $w_b(e, c)$. The value of Φ_i evaluated at vertex c has the special property that $\Phi_i = \mathbf{1}_3 \mathbb{1}_{i=c}$. This allows us to derive the following simplification and solution of Eq. (35), combining both (34.I) and (34.I'):

$$\text{KD}_{j,c} := \begin{bmatrix} B_1(\lambda n_1 + 2\mu n_1) + B_2\mu n_2 + B_3\mu n_3 \\ B_2\mu n_1 + B_1\lambda n_2 \\ B_3\mu n_1 + B_1\lambda n_3 \\ B_2\lambda n_1 + B_1\mu n_2 \\ B_1\mu n_1 + B_2(\lambda n_2 + 2\mu n_2) + B_3\mu n_3 \\ B_3\mu n_2 + B_1\lambda n_3 \\ B_3\lambda n_1 + B_1\mu n_3 \\ B_3\lambda n_2 + B_2\mu n_3 \\ B_1\mu n_1 + B_2\mu n_2 + B_3(\lambda n_3 + 2\mu n_3) \end{bmatrix} \in \mathbb{R}^{3 \times 3} \quad (37)$$

with $B_i := \frac{\partial N_j(x_c)}{\partial x_i}$

$$K_{i,j} = -w_b(e, i) \text{KD}_{j,i} + w_b(e, j) \text{KD}_{i,j}^T. \quad (38)$$

Part (34.II) even simplifies to the following expression:

$$K_{i,j} = -1_{i=j} \eta w_b(e, i) \mathbf{1}_3. \quad (39)$$

B ADDITIONAL ADJOINT CODE EXAMPLE

The adjoint code of the damping parameters is presented here as an example. For a variable x of the forward step, \hat{x} denotes the adjoint/gradient of that variable. One simulation timestep is split as follows:

- (1) Computation of stiffness matrix K .
- (2) Computation of Rayleigh damping matrix $D = \alpha_1 M + \alpha_2 K$ where α_1 and α_2 , respectively, are the damping on mass and stiffness.
- (3) Newmark time integration Eq. (14).

In the adjoint code, these steps are performed in reverse order. One adjoint simulation timestep is split as follows:

- (1) Adjoint of Newmark time integration $\rightarrow \hat{D}$
- (2) Adjoint of Rayleigh damping:

$$\hat{M} = \alpha_1 \hat{D}, \hat{K} = \alpha_2 \hat{D} \quad (40a)$$

$$\hat{\alpha}_1 = \text{vec}(M) \bullet \hat{D}, \hat{\alpha}_2 = \text{vec}(K) \bullet \hat{D}. \quad (40b)$$

- (3) Adjoint of stiffness matrix using \hat{K} among others.

The adjoint variables $\hat{\alpha}_1$ and $\hat{\alpha}_2$ are summed up for every timestep, giving rise to the final gradients for these parameters.

C EXTENDED STABILITY ANALYSIS

In the following we demonstrate the robustness of our solver by comparing reconstructions to synthetic ground truth values.

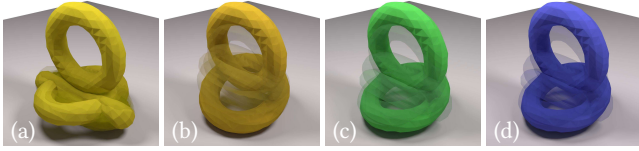


Fig. 17. For different noise and camera settings, our optimizer was used to estimate the torus Young’s modulus. From left to right, images show simulations using the minimal, maximal, reconstructed and ground truth values. Our reconstruction (c) closely matches the ground truth in (d).

C.1 Gradient Stability for Varying Number of Timesteps and Noise

We first investigate the robustness of the gradients computed by our differentiable solver for the SSCs when varying the number of steps over time, and when introducing noise. The following tests are performed with the torus data set shown in Figure 17, and show gradient evaluations when varying the Young’s modulus estimate around a ground truth value of 5000 along the x-axis. I.e. we expect the cost (shown in blue in the following graphs) to have a minimum at 5000, while the gradient (shown in red in terms of its magnitude) should be negative to the left of 5000, and positive on the right side.

The insights we gain from the plots in Figure 18 are twofold: First, the more timesteps are simulated, the more do numerical errors in the adjoint pass accumulate and the noisier the gradients become. Note, however, that the torus a rather difficult test case as it exhibits strong deformations. Despite this effect, the gradients retain the correct sign, i.e., overall direction of the gradient, visible in Figure 18 from the fraction of the red curves above and below the dashed red line. The negative parts lie on the left side of the ground truth value of 5000, while positive gradients lie on the right side. Second, the simulation becomes more stable with increasing noise magnitude. The increase in noise leads to a smoothing of the point assignments, reducing outliers, and hence smoothing the cost function. Furthermore, note that the absolute value of the cost function is larger for higher noise values than for lower ones. This is because even in the optimal case, the observations can be quite far from the surface due to the noise.

C.2 Finite difference based Gradient Estimation

Next, we compare our proposed gradient estimation to a finite-difference based estimation. In particular, we shed light on the influence of finite-difference based gradient estimation using the hyperparameter Δx in the gradient approximation $f'(x) \approx \frac{f(x+\Delta x)-f(x)}{\Delta x}$ on reconstruction accuracy.

Figure 19 plots the cost function and corresponding gradient estimates for the torus test case when varying the Young’s modulus. Especially for a small Δx of 5 units, the resulting gradients exhibit strong noise and a large number of sign flips. This behavior is alleviated for $\Delta x = 100$ in the negative part of the gradient, but remains critical on the positive side (above the ground truth value of 5000). In none of the full optimization runs performed in this work (as presented in the next section, subsection C.4) we were able to reach convergence with the finite difference approach. The adjoint method, in contrast, equipped with our proposed cost function produces numerically stable and smooth results. The corresponding case is shown in the middle column of Fig. 19.

C.3 Influence of Diffusion Distance

The diffusion distance ϕ_{\max} (section 4) specifies the size of the narrow band in the diffusion step, i.e., the maximal distance an observed point can have to the surface to be considered in the optimization. In the following, we investigate its influence on the gradient estimation.

Figure 20 shows the effect of ϕ_{\max} on the cost function and gradient estimates, as well as the reconstructed Young’s modulus. ϕ_{\max} is given in terms of voxels. For small values below 1, only simulation points very close to the observation are used. This introduces additional local minima and leads to gradients with a wrong sign when the current simulation is far from the ground truth (first two plots, left side). Larger values of ϕ_{\max} yield correct gradients for the full range of values, although the quality can deteriorate once values become too large and matching becomes ambiguous. In all of our experiments, we found a value of ϕ_{\max} between 2 and 5 to produce stable and accurate results.

C.4 Optimization Stability Analysis

Next, we consider our full optimization, and compare how the factors previously discussed for gradient estimation influence our full algorithm. We sample 20 random start values for the Young’s modulus and let the optimization find the optimal value.

We first evaluate the influence of the number of different views on the optimization process. The camera locations are randomly sampled on the hemisphere above the ground and focus on the center of the torus. As Figure 21 confirms, almost all runs (95% on average, i.e. 19 out of 20) converge and the number of cameras does not have an influence on stability, even a single camera provides enough observations, and multiple views do not negatively affect the reconstruction quality of our algorithm.

Note that in many case, the Young’s modulus estimates exhibit slight deviations from the ground truth value of 5000. This is caused by the fact that our data generation step relies on triangle surfaces generated with Marching Cubes. The SSC however, directly matches

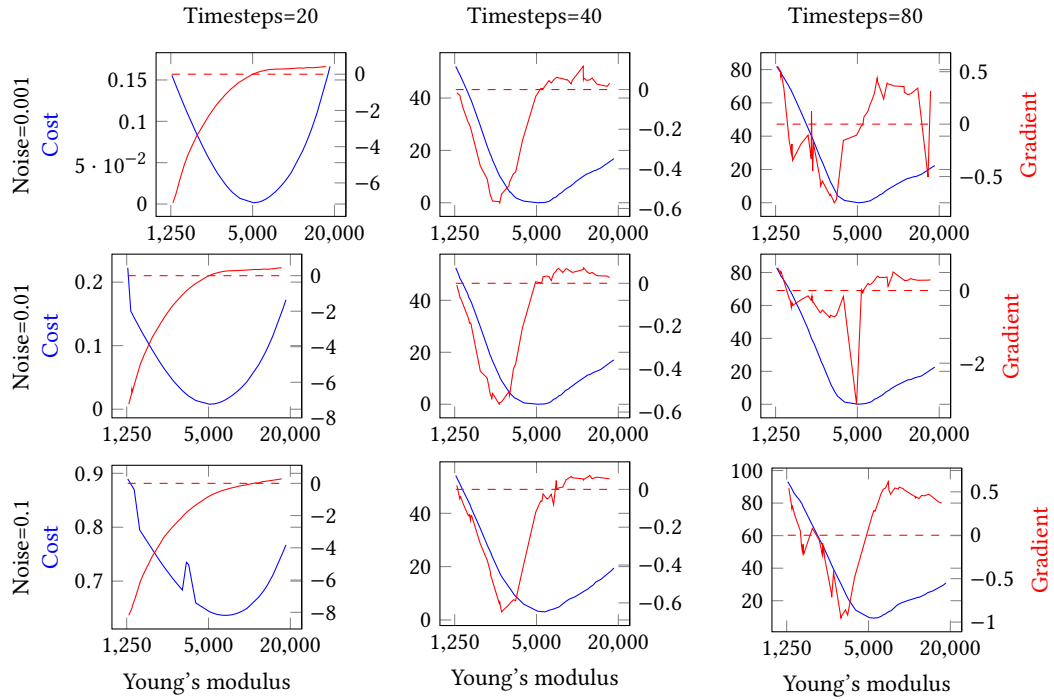


Fig. 18. Influence of number of timesteps and camera noise on the cost function and gradient estimates. Test were performed on the torus data set with $\phi_{\max} = 5$.

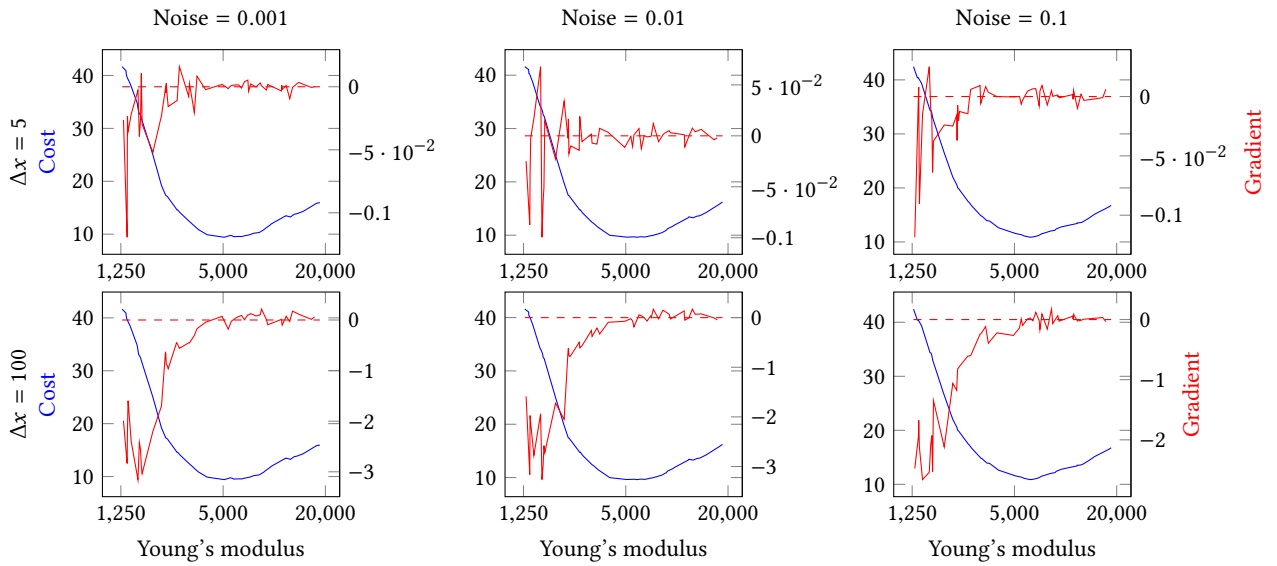


Fig. 19. Comparison between gradient estimation using finite differences and the adjoint method. The test was performed on the torus test case with $\phi_{\max} = 5$ and 40 timesteps.

The jaggedness of the red curves, and especially the large number of sign flips visually indicate that the finite-difference approach is not suitable for optimizations.

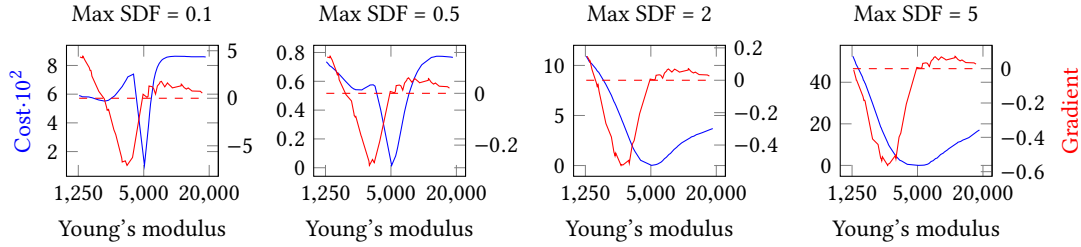


Fig. 20. Influence of diffusion distance ϕ_{\max} on cost function and gradient estimates for the torus data set (Young’s modulus = 5000) with camera noise 0.01 and 40 timesteps.

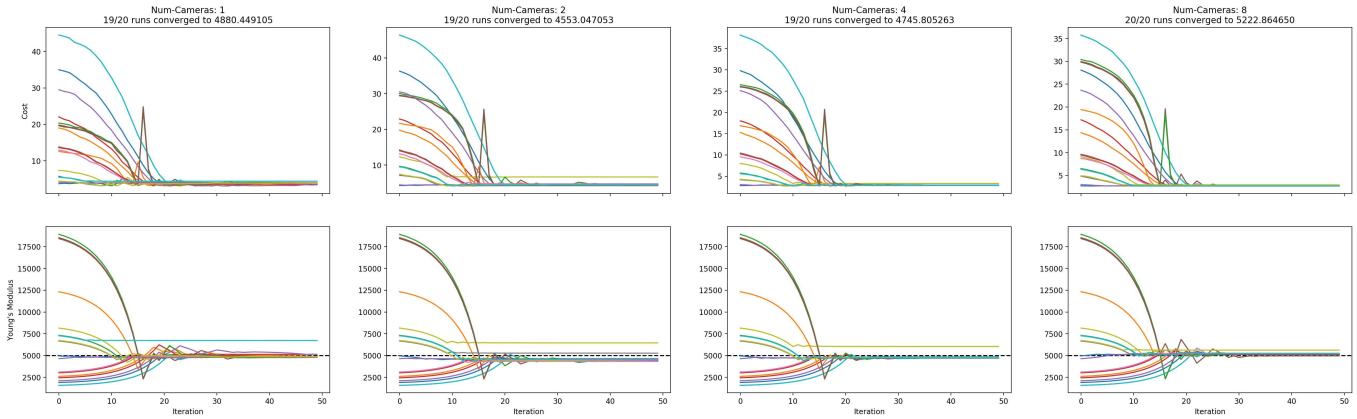


Fig. 21. Influence of number of views on optimization convergence for the torus test case, using 40 timesteps, noise=0.1, maxSdf=5.0, and 20 runs with varying initial Young’s modulus. The average relative error of the converged runs to the ground truth value is 2.39%, 8.94%, 5.08%, 4.46% for 1, 2, 4, 8 cameras, respectively.

tri-linearly interpolated SDF values, which hence cannot be matched exactly in most cases.

The previous results are consistent with those we found when analyzing the influence of the camera resolution on optimization convergence (see Figure 22). For one camera, increasing the resolution, and hence using more points in the cost function, does not improve the optimization.

We also vary the camera noise and diffusion distance, results for which are shown in Figure 23. For a low value for ϕ_{\max} of only one, only 10 of 14 runs converge, the other runs start with a very low Young’s modulus and get stuck. For a value of $\phi_{\max} = 5$, 13 of 14 runs converge to the ground truth. This shows that the convergence rate decreases if the width of the narrow band is chosen too small. In accordance to previous results from the gradient evaluations in subsection C.1, the amount of noise has little influence on the stability of the optimization. The results get slightly better with increased noise (more regularization).

Last, we compare the stability of the algorithm for gradients computed with the adjoint method and for gradients computed with the Finite Different Method and varying Δx , see Figure 24. None of the runs that use the Finite Different Method converge to the Ground Truth value for the Young’s modulus, but rather converge to different local minima away from the ground truth value. This is

in accordance to the gradient analysis in subsection C.2 that show a very noisy behaviour for the gradients. In terms of average relative error, this manifests itself as an error of over 35% for the runs with the finite difference method as compared to 1.41% for the adjoint method

C.5 Stability for Varying Boundary Conditions

To analyze the dependency of the optimization process on the boundary conditions, we use a scene where a ball bounces on the ground plane. Six different settings are used, with randomly sampled orientation and position of the ground plane, and initial linear velocity of the ball, see Figure 25. This leads to strongly differing behavior, i.e., the ball rolling with very different speeds in different directions. For each setting, 20 initial values for the Young’s modulus between 0.1x and 10x the ground truth value of 2000 are randomly sampled. (Same 20 values for each of the six settings). The simulation is performed over 20 timesteps (one bounce), recorded with one virtual camera of resolution 50x50 and a Gaussian noise with variance of 0.07 voxels. The optimization is performed with a maxSDF value of 1 over 30 iterations.

The results are shown in Figure 26. Between 18 and 20 of the 20 initial values converge to the ground truth. Interestingly, for Young’s Moduli smaller than the ground truth, the cost function

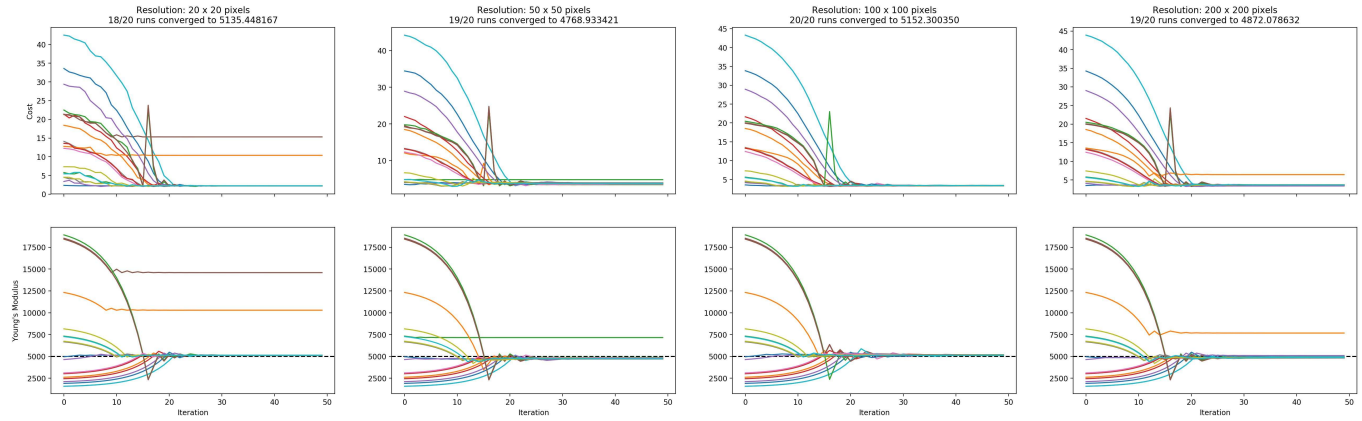


Fig. 22. Influence of camera resolution on optimization convergence for the torus test case, using 40 timesteps, noise=0.1, $\phi_{\max} = 5.0$, 20 runs with varying initial Young's modulus. The average relative error of the converged runs to the ground truth value of 5000 is 2.71%, 4.62%, 3.05%, 2.56% for a resolution of 20^2 , 50^2 , 100^2 , 200^2 , respectively.

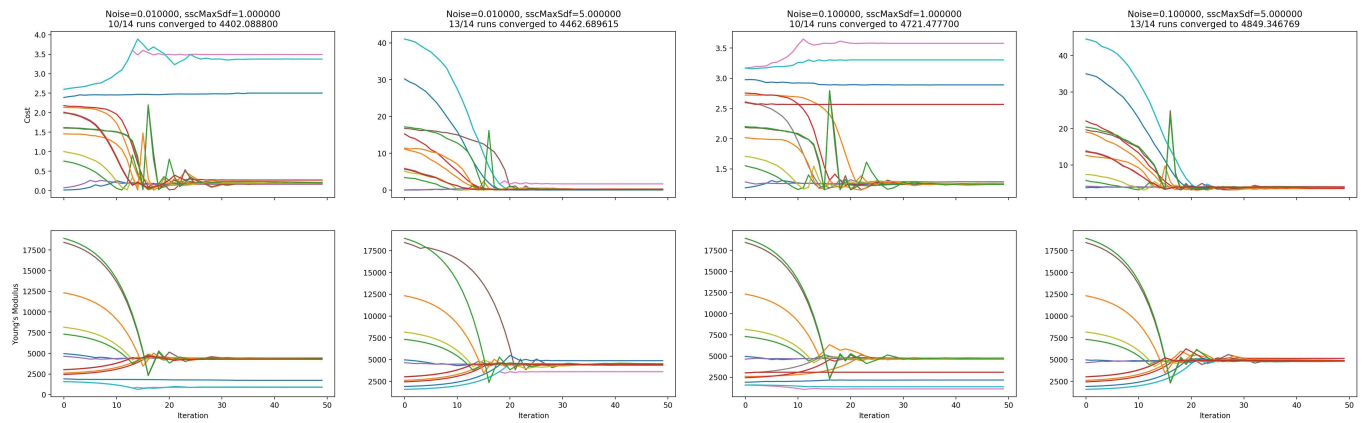


Fig. 23. Influence of ϕ_{\max} and camera noise on optimization convergence for the torus test case, using 40 timesteps and 14 runs with varying initial Young's modulus. The average relative error of the converged runs to the ground truth for the tests from left to right are: 11.96%, 10.75%, 5.57%, 3.01%.

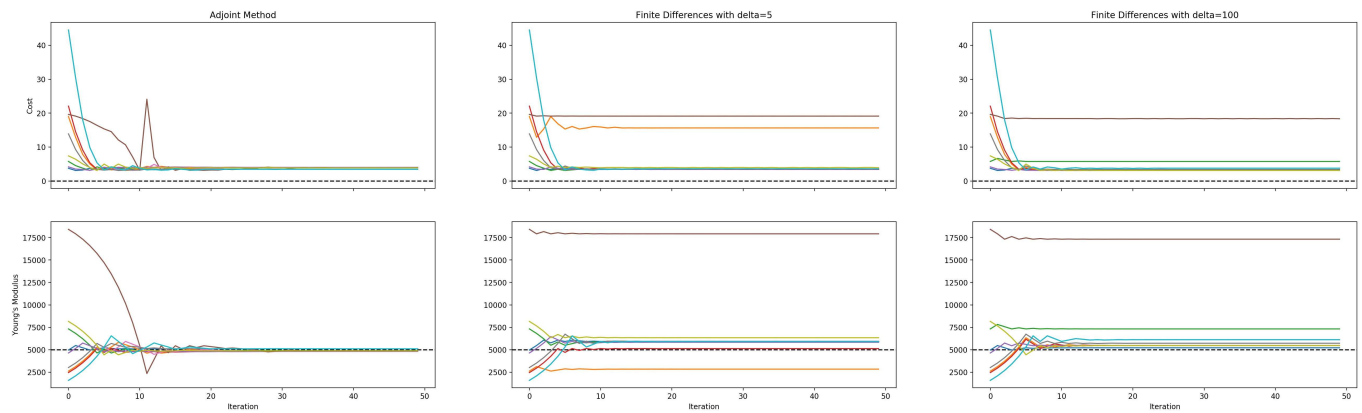


Fig. 24. Comparison of the optimization when the gradients are computed with the adjoint method (left) or with finite differences with different values for Δx . For clarity, only seven runs are shown. Note that none of the runs with finite differences comes close to the ground truth solution. The average relative error of all runs to the ground truth value of 5000 is 1.41%, 35.14%, 39.33% for the adjoint method and finite differences with $\Delta x = 5, 100$, respectively. Especially, runs with initial values that are far away from the ground truth don't converge with the finite differences.

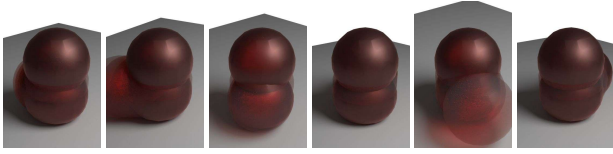


Fig. 25. The six ground orientations used to test the independence of the optimization from boundary conditions. The images show the substantially different collision behavior for each case.

increases first before converging towards zero. This seems to indicate that the gradients from the adjoint method point into the right direction, even though this is not directly reflected in the cost function value. Despite this effect, these tests show that our method also robustly recovers the synthetic ground truth under varying boundary conditions.

C.6 Recovering Multiple Parameters

To analyze the stability of the optimization for multiple parameters, we used the bouncing ball test case again and this time optimize for gravity, the Young’s modulus and stiffness damping. We sampled 60 different initial configurations randomly and let the optimizer run for 20 iterations. The ground truth simulation is shown in Figure 27 on the left. The convergence plots for all 60 runs are shown in Figure 28. As one can see, all runs converge to a solution that has almost zero cost. The reconstructed value for the gravity is quite unique, but a strong inter-dependency between Young’s modulus and stiffness damping is clearly seen. Despite differing values, the reconstructions very closely match the ground truth.

C.7 Different Optimizers

Throughout our work, we use the R-Prop optimizer for the reconstruction. Here we compare it to a simple Gradient Descent optimizer and the L-BFGS optimizer. While R-Prop only uses the sign of the gradient to determine the next search direction, Gradient Descent also uses the norm of the gradient with an additional adaptive step size, so we would expect faster convergence. L-BFGS approximates the Hessian matrix and as a second-order method should converge even faster.

We compared the three optimizers on three different test cases, the fixed Stanford dragon (see Figure 29, the bouncing ball from subsection C.5 and the pillow-ramp test case Figure 15. To clearly see the behaviour of the different optimizers when started from the same initial configurations, we only used one or two runs per setting. The results are shown in Figure 30 and Figure 31.

For the first two test cases, the Dragon and Bouncing Ball, both the R-Prop and the Gradient Descent algorithm converge to a solution (see Figure 29c) that is indistinguishable from the ground truth. Gradient Descent converges faster as expected. The L-BFGS algorithm is often too aggressive in choosing the step size, which leads to the optimization getting stuck in sub-optimal local minima (see Figure 30b. Furthermore, it uses the values of the cost function itself to determine the step size, which can lead to instabilities if the cost function first increases when the solution gets better. This is the case for the bouncing ball test case when started from

a low value for the Young’s modulus, see subsection C.5. These two sources of instability lead to a divergent optimization with the L-BFGS algorithm for the bouncing ball, see Figure 30c.

In the multi-parameters optimization, the Gradient Descent algorithm has severe problems. See e.g. Figure 31 for an example of the Pillow-Ramp test case where the Gradient Descent algorithm completely diverges and leads to a state where the simulation collapses. We believe that this is because Gradient Descent uses the same step size for all parameters. R-Prop and L-BFGS both use a different step size for each parameter. In the test case using the pillow, the L-BFGS starts to oscillate and gets stuck in a sub-optimal local minimum. R-Prop behaves much smoother and finds a good solution.

D REAL WORLD TEST CASES

Here we analyze the convergence of our algorithm for real-world scenarios, as presented in subsection 7.4. Reconstructed parameter values for the best five runs are given in Table 3 for the Teddy, Table 4 for the Pillow-Ramp and Table 5 for the Pillow-Flat data set. Furthermore, Figure 32 shows selected frames and the convergence plots for the Pillow-Flat example.

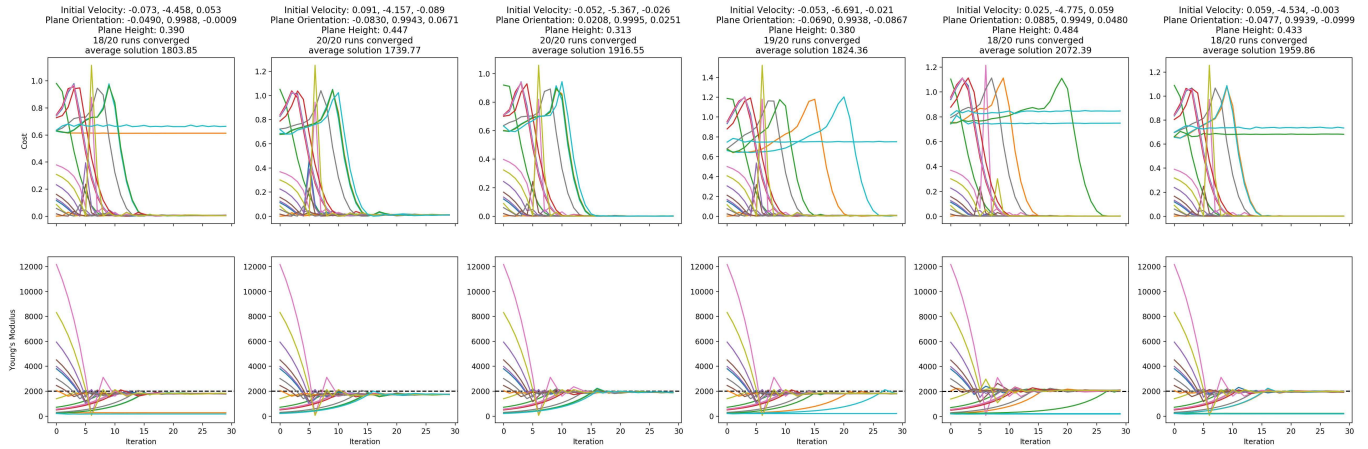


Fig. 26. Same scene, a ball bounces on the floor, with different boundary conditions. Six random settings for the ground plane configuration and initial linear velocity.

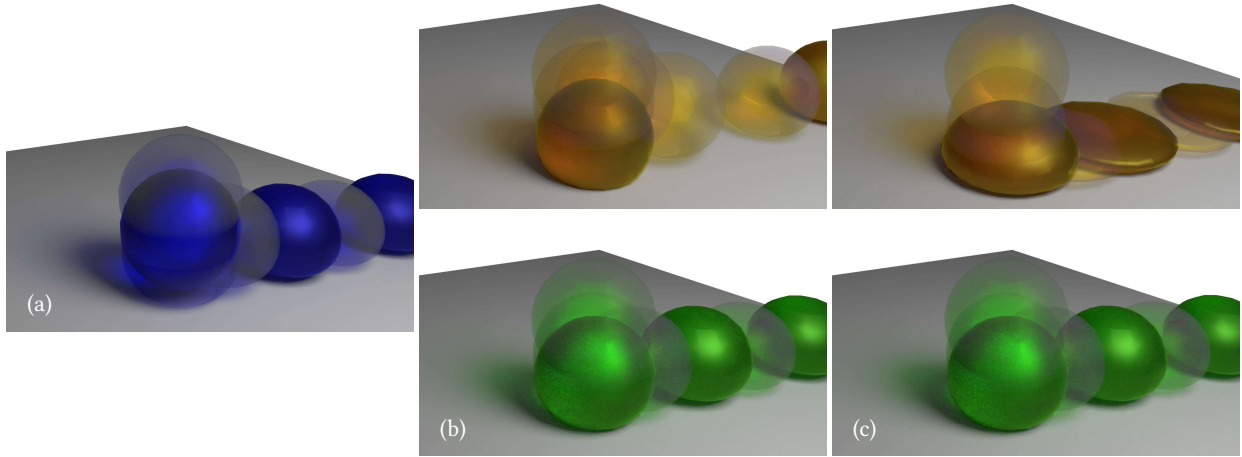


Fig. 27. Multi-parameter optimization for the bouncing ball test case. Ground truth (a) and the initial and reconstruction configuration for the two runs with the highest initial cost (b,c). Even though the reconstructed values are different from the ground truth, the output visually matches the ground truth.

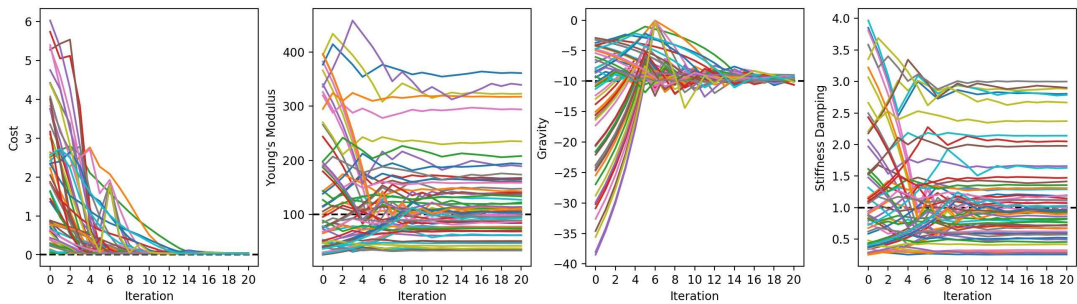


Fig. 28. Bouncing ball, optimized for gravity, Young's modulus and stiffness damping. All 60 initial samples converge to a solution that has almost zero cost and visually same behaviour (see Figure 27). The values for the Young's modulus and stiffness damping, however, strongly differ, showing their inter-dependency.

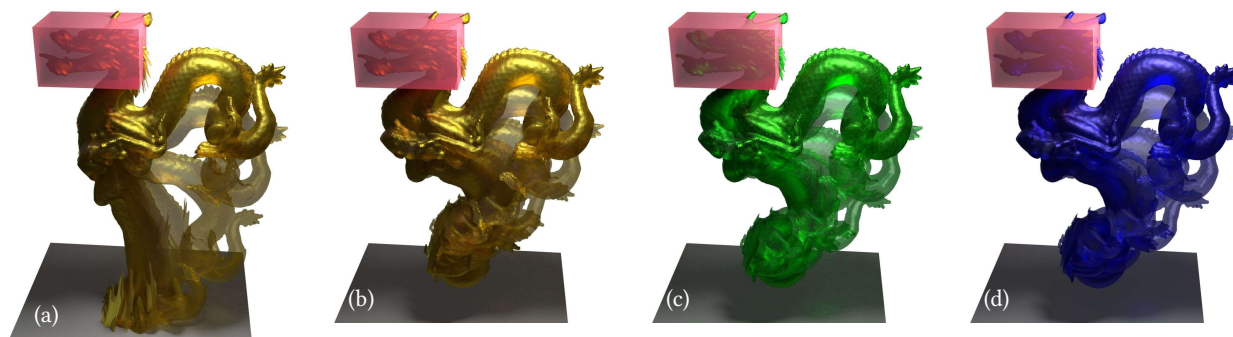


Fig. 29. Optimization of the Young’s modulus on the Dragon. From left to right: minimal and maximal initial value, reconstruction and ground truth.

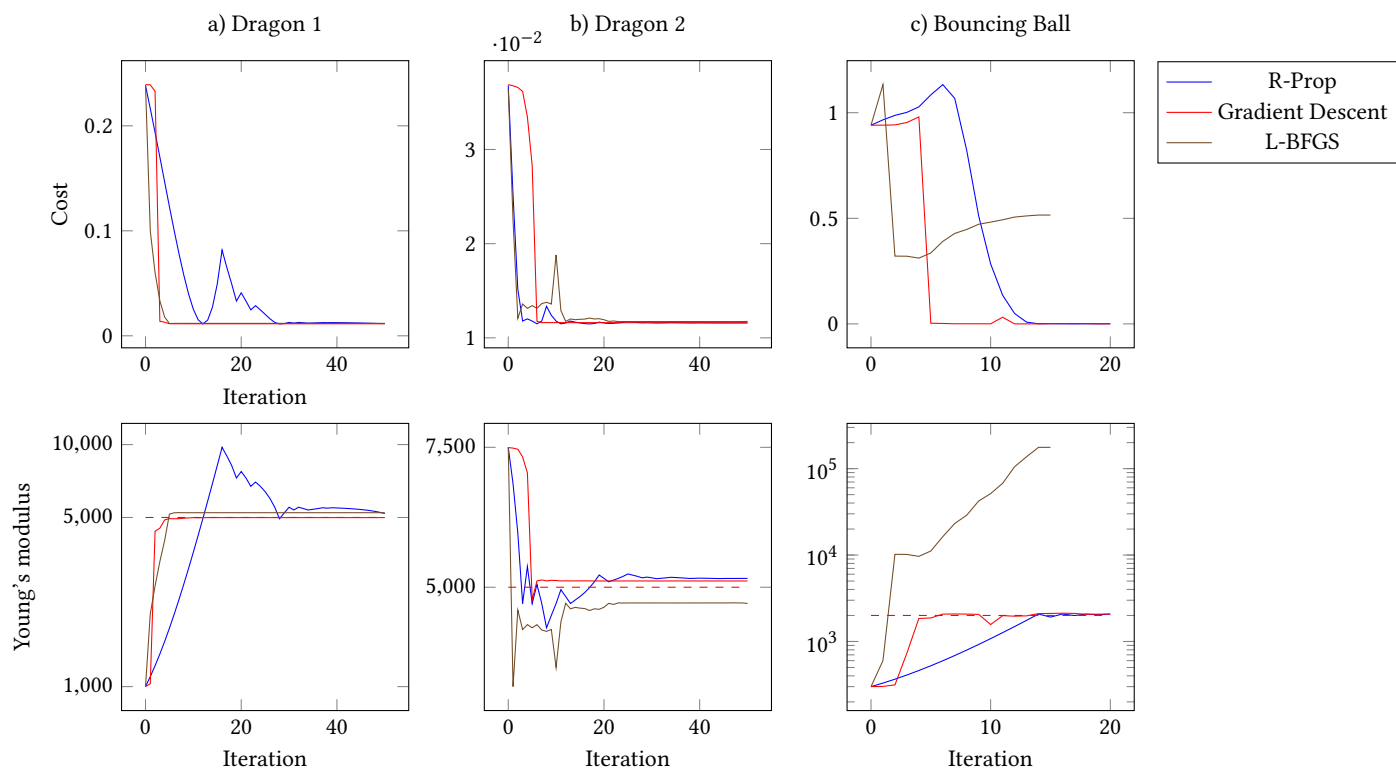


Fig. 30. Comparison of the different optimizers for different scenes.

Run	14	15	18	3	1
Initial Cost	143.924	109.387	134.841	136.685	136.551
Recon. Cost	8.461	8.506	8.693	8.747	8.810
Gravity	-1.536	-1.526	-1.538	-1.521	-1.530
Young’s Modulus	7.817	8.126	8.690	7.840	7.383
Mass Damping	0.240	0.086	0.080	0.122	0.102
Stiffness Damping	0.027	0.033	0.018	0.040	0.043

Table 3. Reconstructed Parameter values from the teddy data set. Only the five best runs are shown.

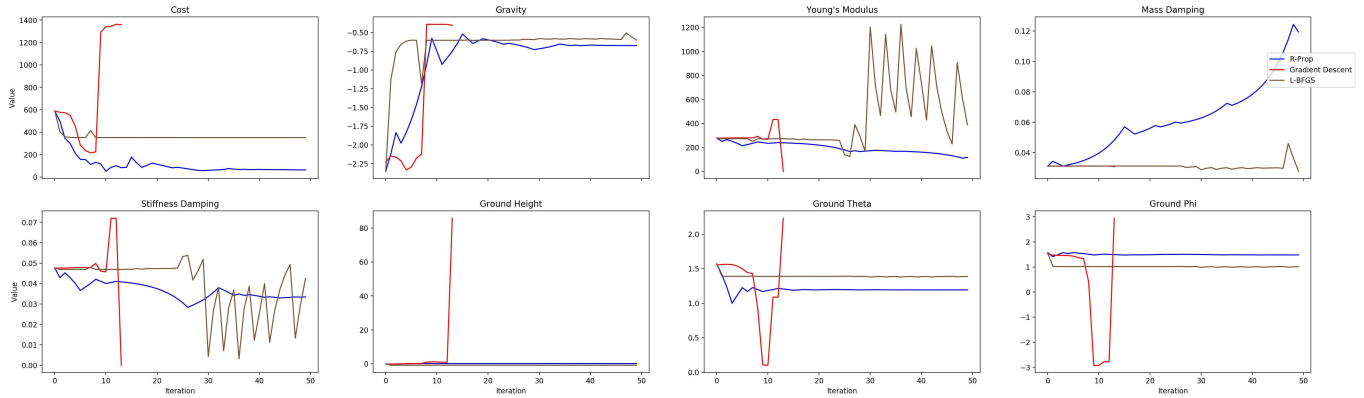


Fig. 31. Comparison of the different optimizers for the Pillow-Ramp example

Run	7	12	4	18	9
Initial Cost	589.252	605.694	550.197	402.254	383.658
Recon. Cost	59.816	91.852	125.231	164.708	170.164
Gravity	-0.710	-1.430	-1.681	-0.805	-1.573
Young's Modulus	209.421	142.042	914.497	839.310	1143.883
Mass Damping	0.068	0.064	0.071	0.176	0.044
Stiffness Damping	0.044	0.082	0.864	0.176	0.184
Ground Height	0.127	0.179	0.181	-0.009	0.009
Ground Theta	1.188	1.229	1.034	1.288	1.222
Ground Phi	1.480	1.226	1.622	1.502	1.466

Table 4. Reconstructed Parameter values from the Pillow-Ramp data set. Only the five best runs are shown.

Run	8	7	3	5	2
Initial Cost	249.871	154.268	456.128	587.173	116.719
Recon. Cost	21.126	29.303	30.233	34.395	48.241
Gravity	-0.872	-0.883	-1.031	-1.017	-1.038
Young's Modulus	9.200	37.206	233.827	9.191	18.835
Mass Damping	0.078	0.051	0.119	0.425	0.046
Stiffness Damping	0.015	0.008	0.011	0.014	0.011

Table 5. Reconstructed Parameter values from the Pillow-Flat data set. Only the five best runs are shown.



(a) Color Observation



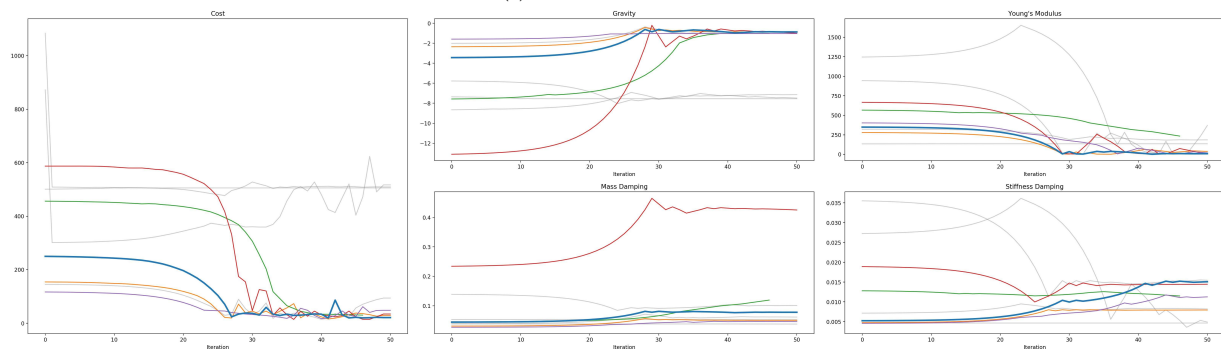
(b) Depth Observation



(c) Initial configuration for the optimization



(d) Reconstructed solution



(e) Optimization started from 10 different initial values. The best five runs are drawn in color, the very best run is drawn in thick lines and displayed in the renderings above.

Fig. 32. Selected frames and plots of the optimization process for the Pillow-Flat test case. The rows of (a-d) each show a sequence of steps over time.